Theory and Practice of Ceramic Processes

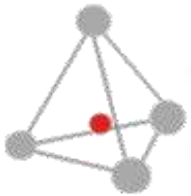

Sintering of Ceramic Powders

Waldemar Pyda

Scope:
Sintering
Breaking-down processes

AGH

Categories of Sintering

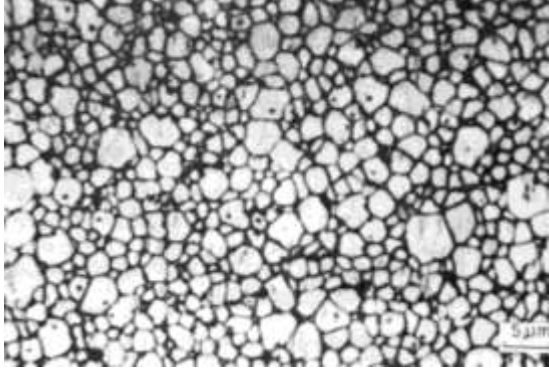

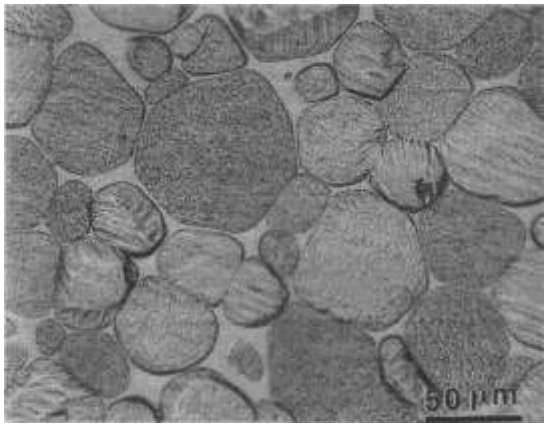

Solid-state sintering: the shaped green body is heated to a temperature that is typically 0.5–0.9 of the melting point. No liquid is present and atomic diffusion in the solid state produces joining of the particles and reduction of the porosity.

Liquid-phase sintering: a small amount of liquid, typically less than a few volume percent of the original solid mixture, is present at the sintering temperature. The liquid volume is insufficient to fill the pore space so that additional processes are required to achieve full densification. Liquid-phase sintering is an important method for the industrial fabrication of many ceramics. While the liquid phase can allow enhanced densification at lower temperatures, a difficulty, particularly in the case of ceramics for structural applications, is that the maximum use temperature of the material may be controlled by the softening temperature of the solidified liquid phase.

Vitrification: for a mixture where a relatively large volume of liquid (typically greater than ~25% of the original solid volume) is formed on heating, the liquid volume is sufficient to fill the volume of the remaining pores. Thus, a dense product can be achieved by the formation of the liquid, flow of the liquid into the pores, and either crystallization or vitrification (glass formation) of the liquid on cooling. Vitrification is particularly important for the production of ceramics from naturally available raw materials such as clays.

Viscous sintering: a consolidated mass of glass particles is heated near to, or above its softening temperature. Densification occurs by viscous flow of the glass under the influence of surface tension.

Selected materials and connected sintering processes

Composition	Sintering process	Application
Al_2O_3	Solid-state sintering with MgO additive	Sodium vapor arc lamp tubes
	Liquid-phase sintering with a silicate glass	Furnace tubes; refractories
MgO	Liquid-phase sintering with a silicate glass	Refractories
Si_3N_4	Liquid-phase sintering with oxide additives (e.g. Al_2O_3 and Y_2O_3) under nitrogen gas pressure or under an externally applied pressure	High-temperature structural ceramics
SiC	Solid-state sintering with B and C additives; liquid-phase sintering with Al, B and C or oxide additives	High-temperature structural ceramics
ZnO	Liquid-phase sintering with Bi_2O_3 and other oxide additives	Electrical varistors
$BaTiO_3$	Liquid-phase sintering with TiO_2-rich liquid	Capacitor dielectrics; thermistors
$Pb(Zr,Ti)O_3$ (PZT), $(Pb,La)(Zr,T)O_3$ (PLZT)	Sintering with a lead-rich liquid phase; hot pressing	Piezoelectric actuators and electro-optic devices
ZrO_2/(3–10 mol% Y_2O_3)	Solid-state sintering	Electrical conducting oxide for fuel cells
Mn–Zn and Ni–Zn ferrites	Solid-state sintering under a controlled oxygen atmosphere	Soft ferrites for magnetic applications
Porcelain	Vitrification	Electrical insulators; tableware
SiO_2 gel	Viscous sintering	Optical devices

SOLID-STATE SINTERING

Driving forces

The specific energy and curvature of the particle surfaces provide an effective stress on the atoms under the surface. For a curved surface with principal radii of curvature r_1 and r_2, this stress is given by the equation of Young and Laplace:

$$\sigma = \gamma_{sv}\left(\frac{1}{r_1} + \frac{1}{r_2}\right) \quad (1)$$

where γ_{sv} is the specific surface energy. The *diffusion potential*, μ, which drives matter transport is in this case found by equating the mechanical work performed by the stress to the thermodynamic work required for the reduction of the surface free energy. A commonly used relation is

$$\mu = \sigma\Omega \quad (2)$$

where Ω is the atomic or molar volume. The equation for μ is actually more complex for polycrystalline ceramics where the pores are in contact with the grain boundaries [4].[1] For example, in the final stage of sintering where the pores are assumed to be spherical, one expression is [5]:

$$\mu = \Omega\left(\frac{2\gamma_{gb}}{G} + \frac{2\gamma_{sv}}{r}\right) \quad (3)$$

where γ_{gb} is the specific energy of the grain boundary, G is the diameter of the grains, and r is the radius of the pores. According to Eq. 3, the chemical potential consists of two contributions, one attributed to the pores and the other attributed to the boundaries.

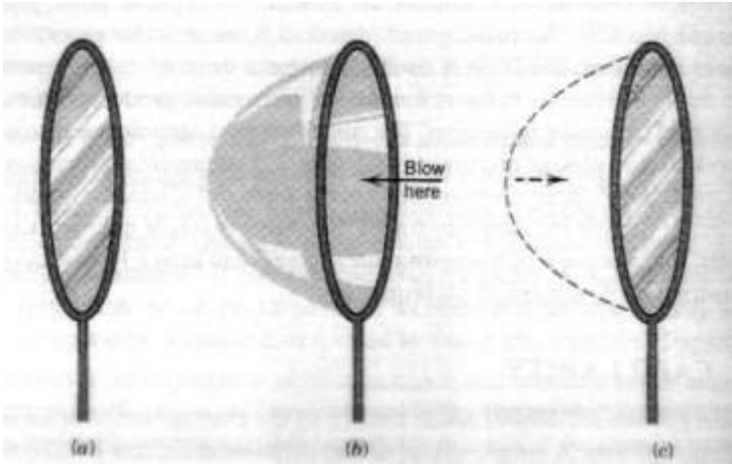

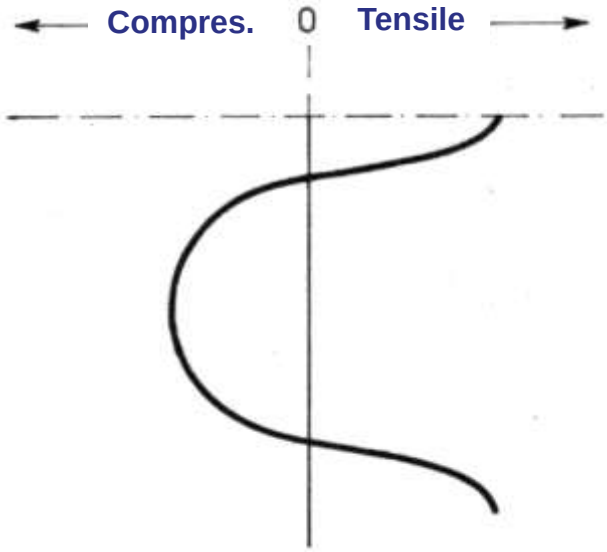

Stresses induced in the neck

Determination of radia of curvature

$$\Delta P = \gamma' \left(\frac{1}{R_1} + \frac{1}{R_2} \right)$$

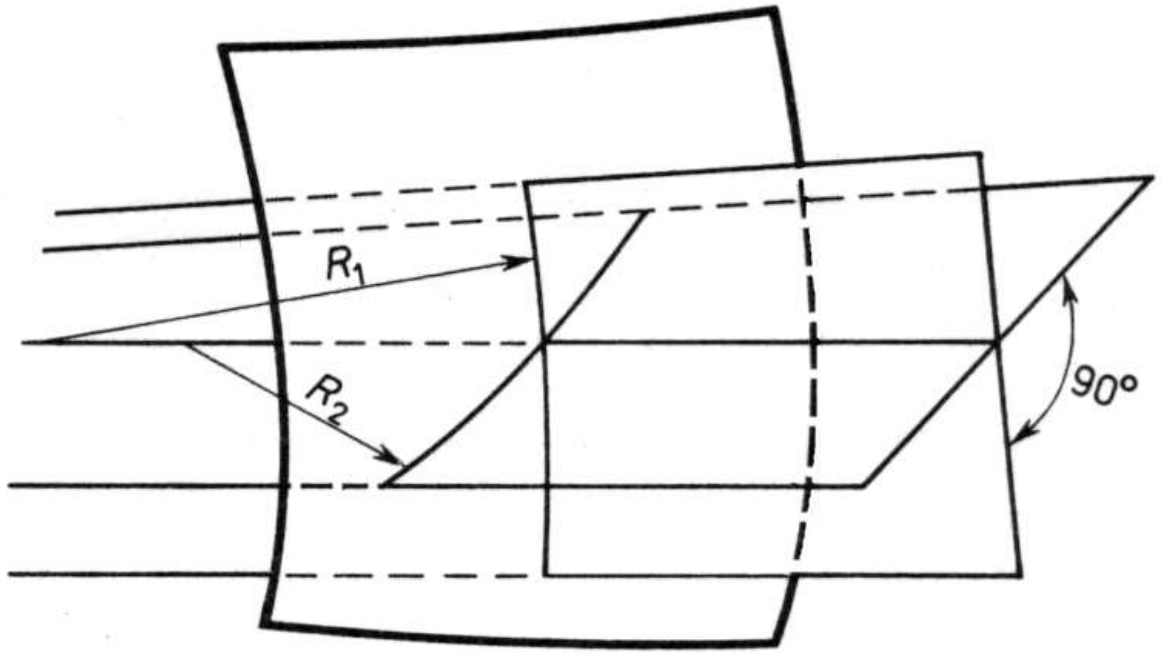

Mechanisms of sintering

Mechanisms
1. Surface diffusion
2. Lattice diffusion (from the surface)
3. Vapor transport
4. Grain boundary diffusion
5. Lattice diffusion (from the grain boundary)
6. Plastic flow (by dislocation motion)

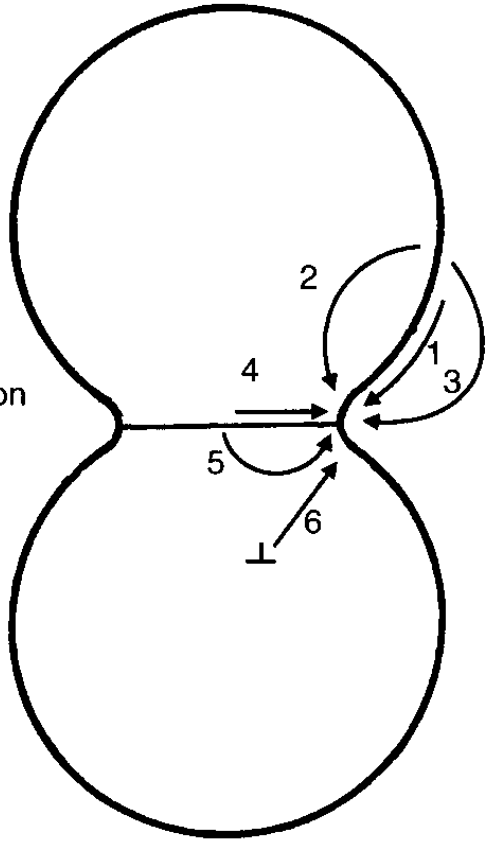

Non-densifying mechanisms 1, 2, and 3 produce microstructural change without causing shrinkage

Densifying mechanisms 4, 5, and 6 remove material from the grain boundary region leading to shrinkage

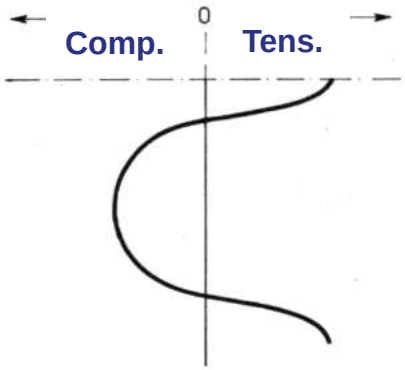

$$\Delta P = \gamma' \left(\frac{1}{R_1} + \frac{1}{R_2} \right)$$

$$[V_{\text{ścisk.}}] = [V_0] \left(1 - \frac{\sigma \Omega_v}{kT} \right)$$

$$[V_{\text{rozc.}}] = [V_0] \left(1 + \frac{\sigma \Omega_v}{kT} \right)$$

Stages of sintering

The *initial stage* would begin as soon as some degree of atomic mobility is achieved and, during this stage, sharply concave necks form between the individual particles. The amount of densification is small, typically the first 5% of linear shrinkage, and it can be considerably lower if coarsening mechanisms are very active. In the *intermediate stage*, the high curvatures of the initial stage have been moderated and the microstructure consists of a three-dimensional interpenetrating network of solid particles and continuous, channel-like pores. This stage is considered valid to ~5–10% porosity and therefore covers most of the densification. Grain growth (coarsening) starts to become significant. As sintering proceeds, the channel-like pores break down into isolated, closed voids, which marks the start of the *final stage*. Grain growth can be more extensive in the final stage and difficulties are commonly encountered in the removal of the last few percent of porosity.

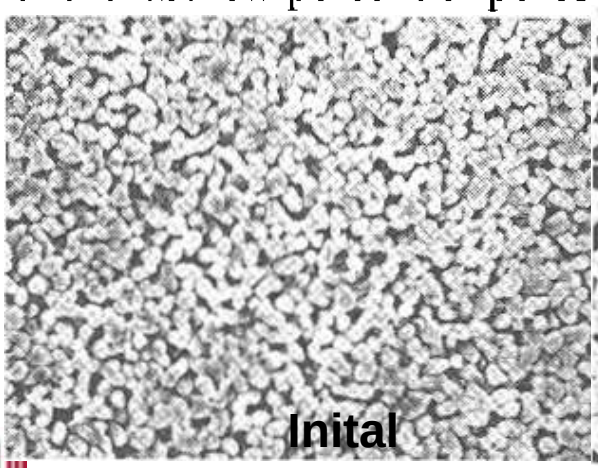

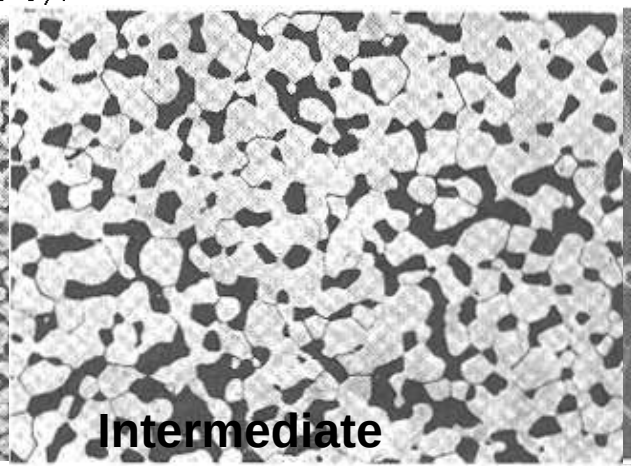

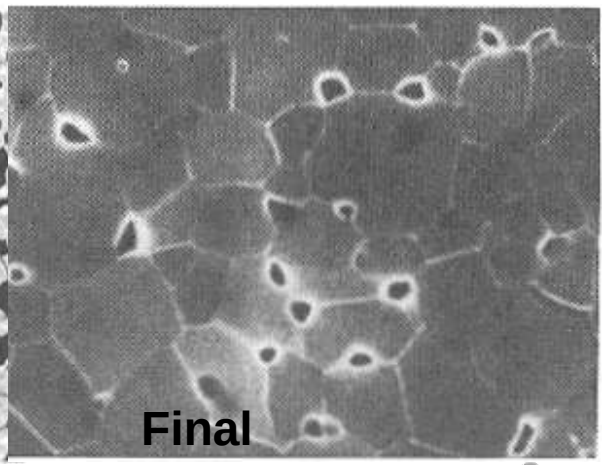

Stages of sintering – a model

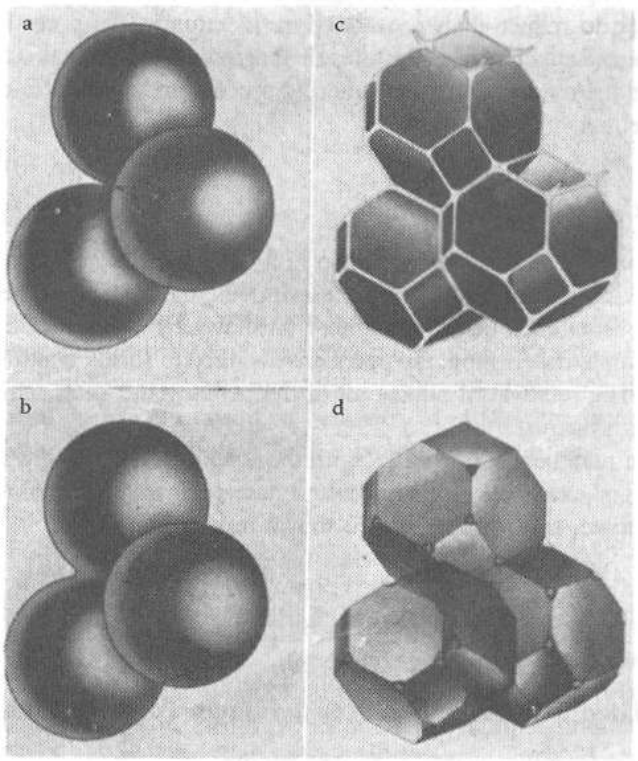

Idealized models for the three stages of sintering. (a) Initial stage: model structure represented by spheres in tangential contact. (b) Near the end of the initial stage: spheres have begun to coalesce. The neck growth illustrated is for center-to-center shrinkage of 4%. (c) Intermediate stage: dark grains have adopted the shape of a tetrakaidecahedron, enclosing white pore channels at the grain edges. (d) Final stage: pores are tetrahedral inclusions at the corners where four tetrakaidecahedra meet. (From Coble, R.L., Sintering crystalline solids. I. Intermediate and final state diffusion models. *J. Appl. Phys.*, 32, 787, 1961. With permission.)

Competition between densification and sintering

The various sintering mechanisms do not operate independently. Vapor transport and surface diffusion compete with the densifying mechanism. They lead to coarsening of the microstructure and a reduction of the driving force for sintering, so that a significant reduction in the densification rate can result. Sintering is, therefore, said to involve a competition between densification and coarsening. The production of ceramics with high density (Fig. 4.1.2a) would require choosing the sintering conditions so that the non-densifying mechanisms are not very active (see Section 4.1.7). When coarsening mechanisms dominate, the production of a highly porous body is favored (Fig. 4.1.2b).

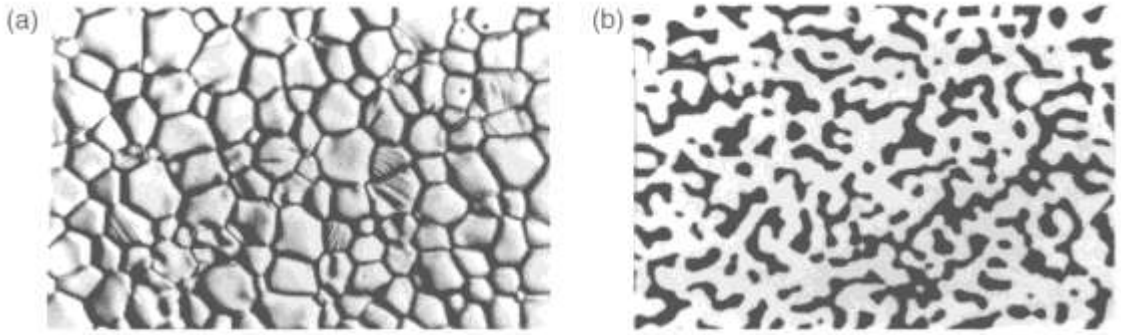

FIGURE 4.1.2 (a) The surface of an Al_2O_3 ceramic from which all porosity has been removed during sintering in which the densifying processes dominate. (b) The sintering of silicon where coarsening mechanisms dominate results in formation of a continuous network of solid material (white) and porosity (black). The microstructural change is not accompanied by any densification. (From Brook, R. J. (1991). *Concise Encyclopedia of Advanced Ceramics*. With kind permission of Elsevier, Oxford.)

Effects of grain boundaries

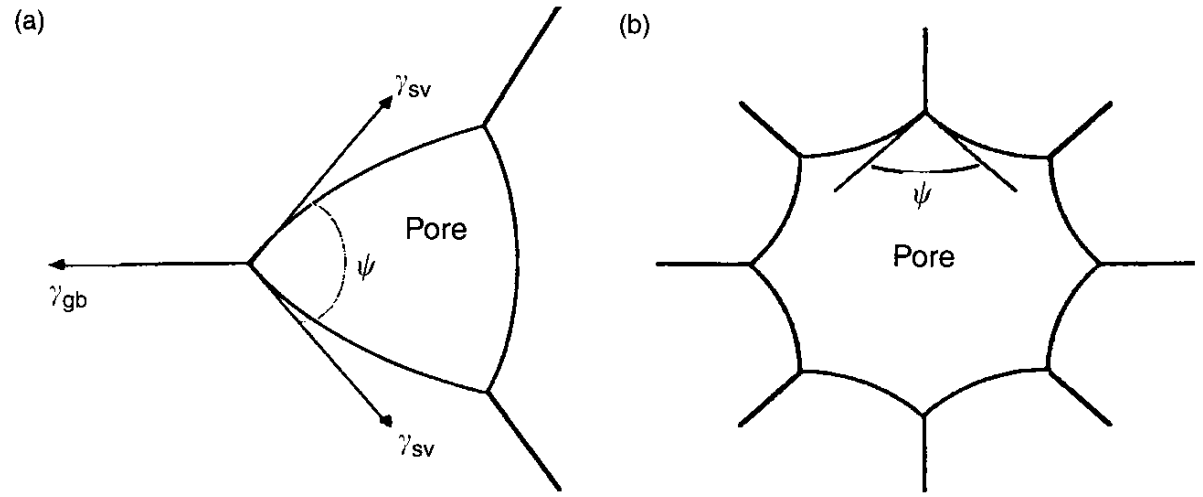

FIGURE 4.1.3 Pore shape and pore stability are determined by the dihedral angle and the pore coordination number: (a) The pore with the concave surfaces will shrink while (b) the pore with the convex surfaces will grow (or become metastable).

shown in Figure 4.1.3a this balance of forces leads to

$$\cos\left(\frac{\psi}{2}\right) = \frac{\gamma_{gb}}{2\gamma_{sv}} \tag{5}$$

where ψ is the dihedral angle, γ_{gb} is the specific grain boundary energy, and γ_{sv} is the specific surface energy.

Pore stability during sintering

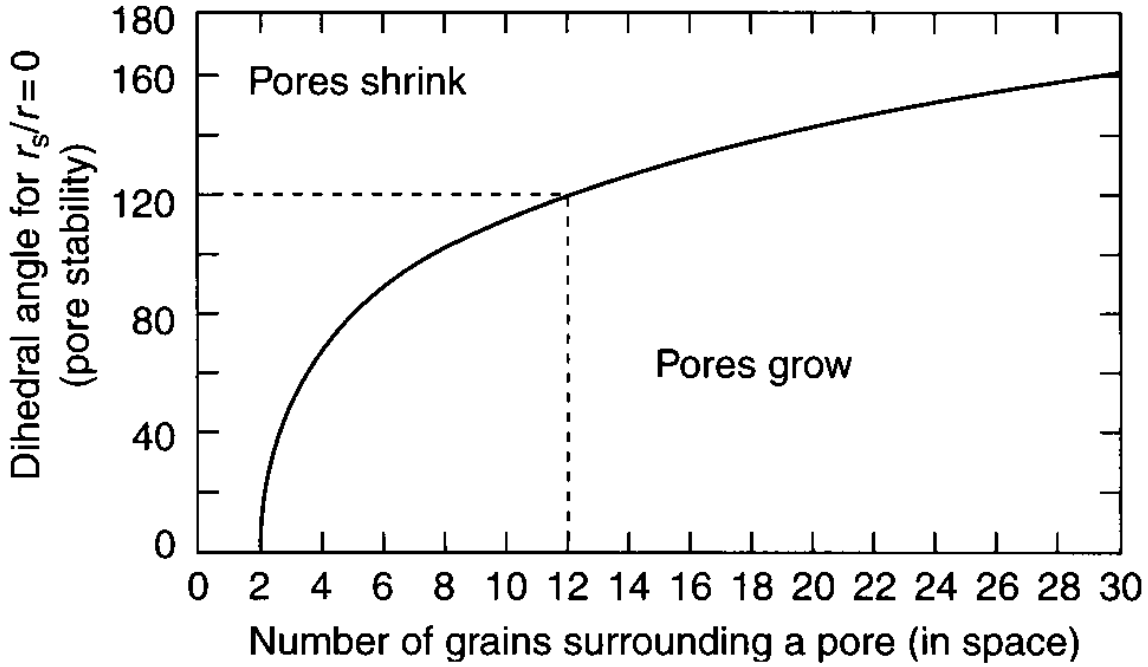

FIGURE 4.1.4 Conditions for pore stability as a function of pore coordination number and dihedral angle. For a dihedral angle of 120°, pores surrounded by more than 12 grains will grow (from Ref. [16]).

Sintering models

Analytical models

For any stage of the sintering process, the model predictions for the densification rate, $\dot{\varepsilon}_\rho = (1/\rho)\,\mathrm{d}\rho/\mathrm{d}t$, can be expressed in general form [1, 2]:

$$\dot{\varepsilon}_\rho = \left(\frac{1}{\rho}\right)\frac{\mathrm{d}\rho}{\mathrm{d}t} = \frac{HD\Omega\phi^{(m+1)/2}}{G^m kT}(p_a + \Sigma) \qquad (6)$$

where H is a numerical constant that depends on the assumed geometry of the model and on the sintering mechanism, Ω is the atomic volume of the rate controlling species, G is the grain (or particle) size, k is the Boltzmann constant, and T is the absolute temperature. The diffusion coefficient D and the grain size exponent, m, take on their appropriate values for a given mechanism: $D = D_l$ and $m = 2$ for lattice diffusion, where D_l is the lattice diffusion coefficient; $D = D_{gb}\delta_{gb}$ and $m = 3$ for grain boundary diffusion, where δ_{gb} is the grain boundary thickness. The term Σ is the sintering stress, defined earlier as the *equivalent externally applied stress* that has the same effects on sintering as the curved surfaces of pores and grain boundaries. The term ϕ, referred to as the *stress intensification factor*, is a geometrical parameter that relates the externally applied stress to the actual stress on the grain boundaries

Herring's Scalling Law

Herrings scaling law does not assume a specific geometrical model. Instead, it assumes that the geometrical changes remain similar. The law considers the effect of change of scale (e.g. particle size) on the rate of matter transport for individual mechanisms. The times for equivalent geometric change can be expressed as:

$$\frac{t_2}{t_1} = \left(\frac{G_{2,0}}{G_{1,0}}\right)^m \tag{7}$$

where the subscripts 1 and 2 represent two different powders with initial particle size $G_{1,0}$ and $G_{2,0}$, respectively and m is an integer that depends on the mechanism of matter transport: $m = 4$ for surface diffusion and for grain boundary diffusion, $m = 2$ for vapor transport, and $m = 3$ for lattice diffusion.

Sintering Stress

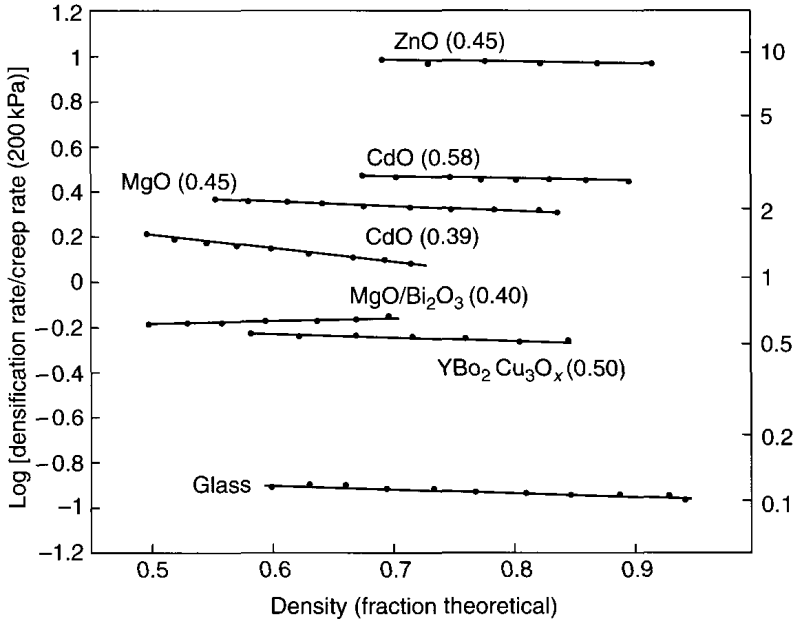

FIGURE 4.1.5 The ratio of the densification rate to the creep rate at a constant stress (0.2 MPa) for various ceramics and for glass. The numbers in parentheses are the initial densities (from Ref. [36]).

In the loading dilatometry experiments, the hydrostatic component of the applied uniaxial stress is small compared to the sintering stress, so that the sintering mechanism of the loaded powder compact is expected to be identical to that for a freely sintered compact. Equation 6 can be written as [1, 2]

$$\dot{\varepsilon}_\rho = \frac{HD\Omega\phi^{(m+1)/2}}{G^m kT}\Sigma \tag{8}$$

Assuming the same mechanism for creep under the low uniaxial stress, p_z, an equation for the creep rate is

$$\dot{\varepsilon}_c = \frac{H'D\Omega\phi^{(m+1)/2}}{G^m kT}p_z \tag{9}$$

where H' is a numerical constant. The ratio of the densification rate to the creep rate can be found from Eqs 8 and 9 as

$$\frac{\dot{\varepsilon}_\rho}{\dot{\varepsilon}_c} = \frac{F\Sigma}{p_z} \tag{10}$$

where F is a constant. Measurement of the densification rate and the creep rate at a fixed value of p_z for identical samples indicates that the ratio $\dot{\varepsilon}_\rho/\dot{\varepsilon}_c$ is fairly constant over a wide density range for several materials (Fig. 4.1.5).

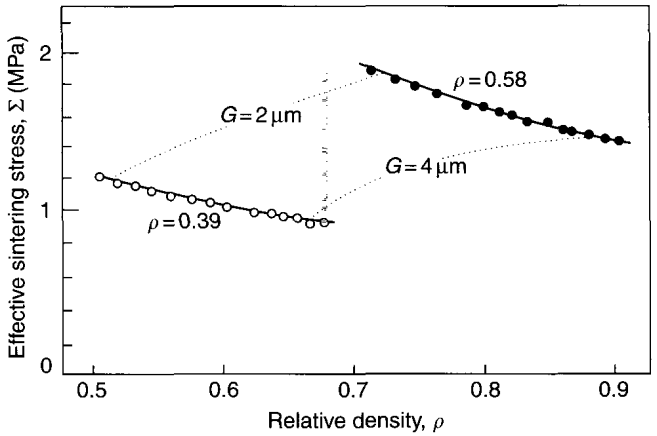

FIGURE 4.1.6 Sintering stress versus relative density for CdO powder compacts of two different initial densities ρ (from Ref. [34]).

The Stress Intensification Factor

Solid-state sintering involves atomic transport from the grain boundaries to fill up the pores and is dependent on the *effective stress* on the grain boundaries. We therefore require a way to relate the externally applied stress, σ_a, to the effective stress on the grain boundary, σ_e. This has been commonly achieved (see Eq. 6) by using a parameter, ϕ, referred to as the *stress intensification factor*, that depends on the geometry of the porous compact:

$$\sigma_e = \sigma_a \phi \tag{11}$$

The stress intensification factor is equal to the ratio of the total cross-sectional area (of the solid phase plus the pores), A_t, to the effective cross-sectional area (of the solid-phase only), A_e. For a polycrystalline material, ϕ is equal to the cross-sectional area of the grain, A_g, divided by the grain boundary area, A_{gb}:

$$\phi = \frac{A_t}{A_e} = \frac{A_g}{A_{gb}} \tag{12}$$

If the pores are spherical and randomly distributed through the porous compact, such as a glass in the final stage of sintering, ϕ takes a simple form [21]:

$$\phi = 1/\rho \tag{13}$$

where ρ is the relative density of the compact. In general, the relationship may be expected to be complex. However, computer calculations by Beere [40] on the equilibrium shapes of pores in a porous compact yield results that can be well fitted to simple analytical expressions. One expression is [41]

$$\phi = \exp[a(1-\rho)] \tag{14}$$

where a is a constant that depends on the dihedral angle of the pores (Fig. 4.1.2). Data for the creep rates of some porous compacts measured in the loading dilatometry experiments described earlier [34, 35] yield values for ϕ that can be well fitted by Eq. 14. An example of such data is shown in Figure 4.1.7 for CdO.

Normal and abnormal grain growth

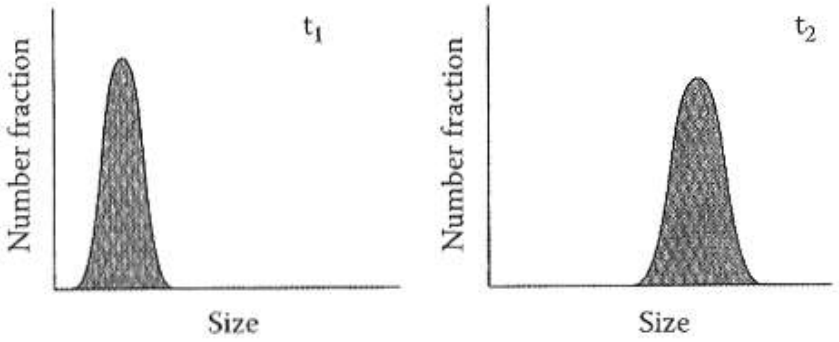

(a) Normal grain growth

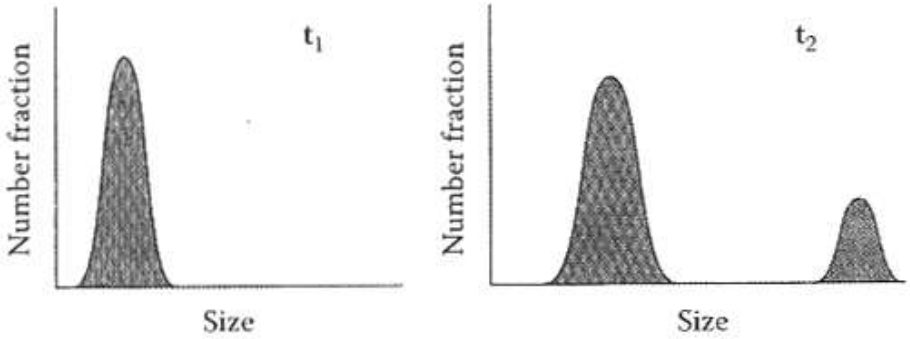

(b) Abnormal grain growth

For an initial microstructure consisting of a unimodal distribution of grain sizes, (a) normal grain growth results in an increase in the average grain size, whereas the grain size distribution remains almost self-similar; (b) abnormal grain growth is characterized by a few large grains growing rapidly at the expense of the surrounding matrix grains and may lead to a bimodal distribution of grain sizes.

Normal Grain Growth

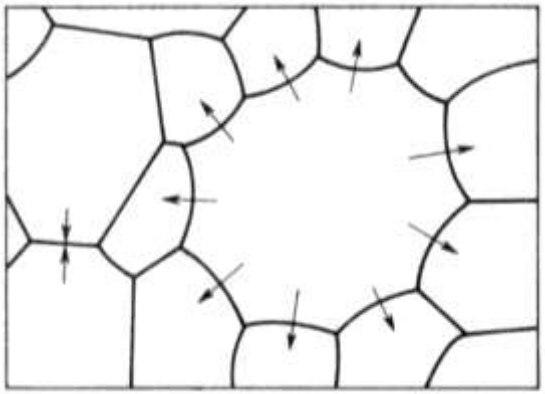

The grain growth models predict a kinetic equation of the form

$$G^m = G_0^m + Kt$$

where G is the grain size at time t, G_0 is the grain size at $t = 0$, and K is a temperature-dependent rate constant obeying the Arrhenius equation. For the Burke and Turnbull model and for the mean field theories, $m = 2$ (i.e. parabolic growth kinetics) while the topological model of Rhines and Craig predicts $m = 3$. A non-integral value of $m = 2.44$ has been obtained in the computer simulation depicted in Figure 4.1.8. In practice, grain growth data for dense ceramics yield m values ranging from 2 to 4.

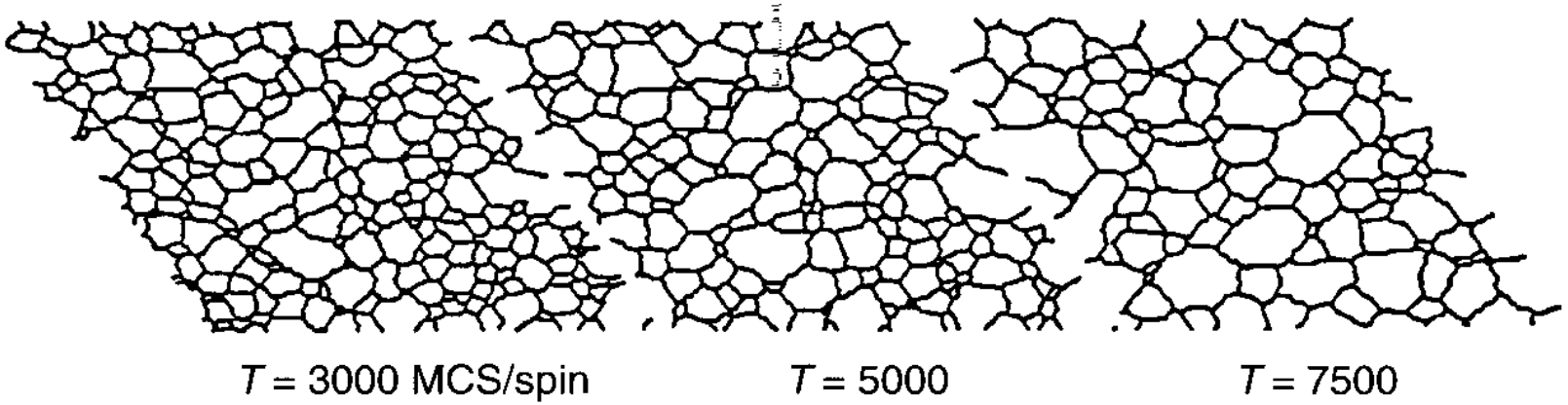

FIGURE 4.1.8 Grain growth in a dense polycrystalline solid determined by computer simulation employing a Monte Carlo method (from Ref. [51], with kind permission of Elsevier, Oxford).

Abnormal Grain Growth

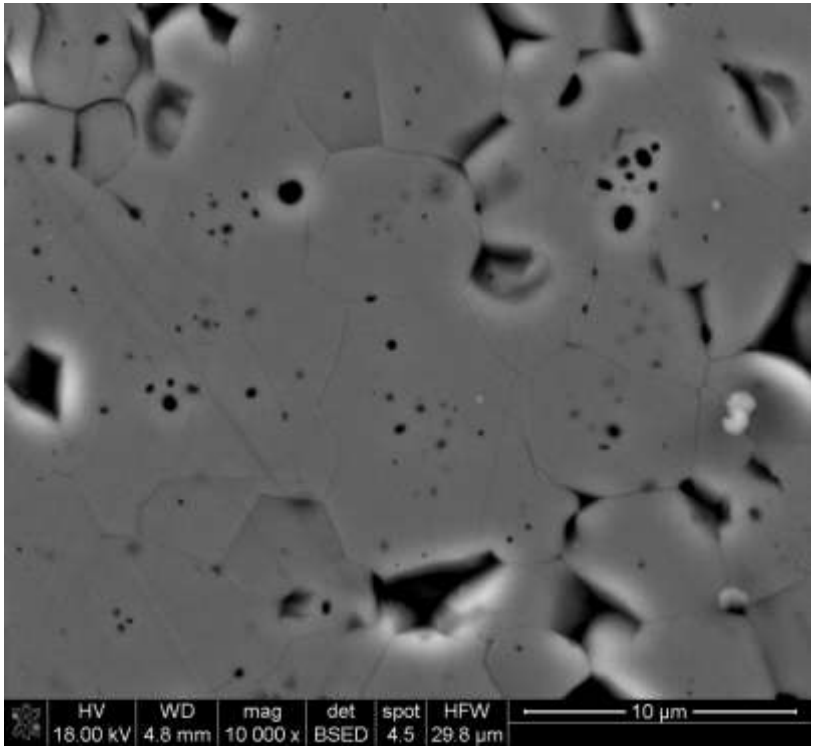

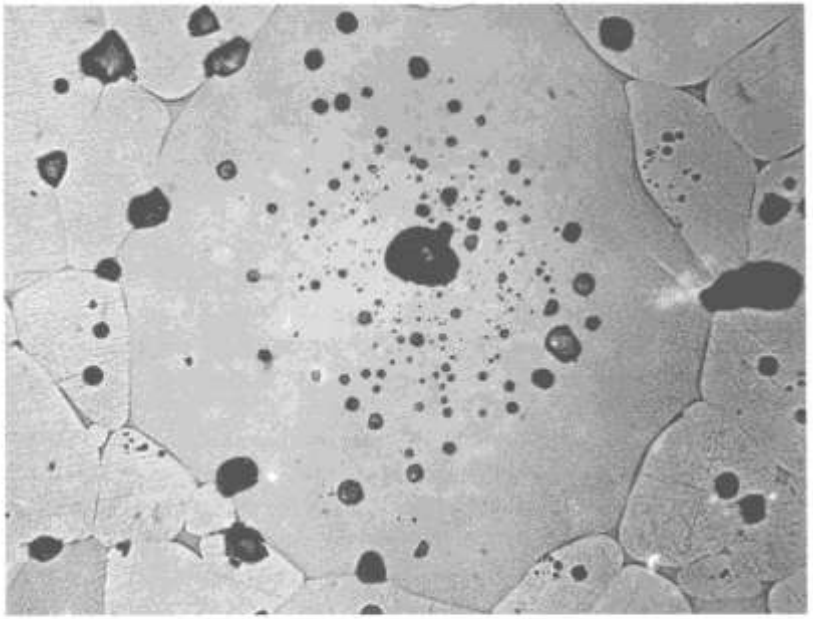

Abnormal grain growth in an MgO ceramic. The pores trapped inside the abnormal grain are difficult to remove, thereby leading to residual porosity in the sintered material (magnification = 700).

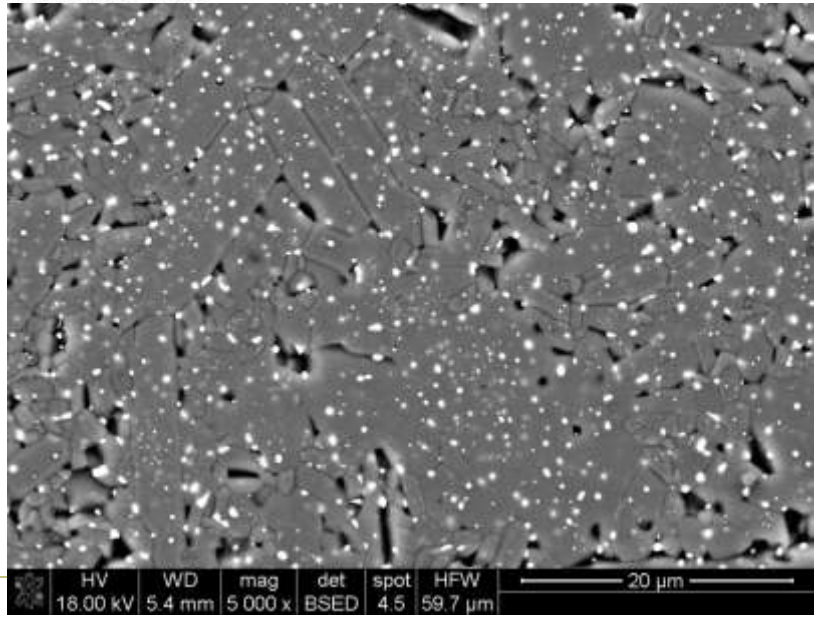

Abnormal Grain Growth

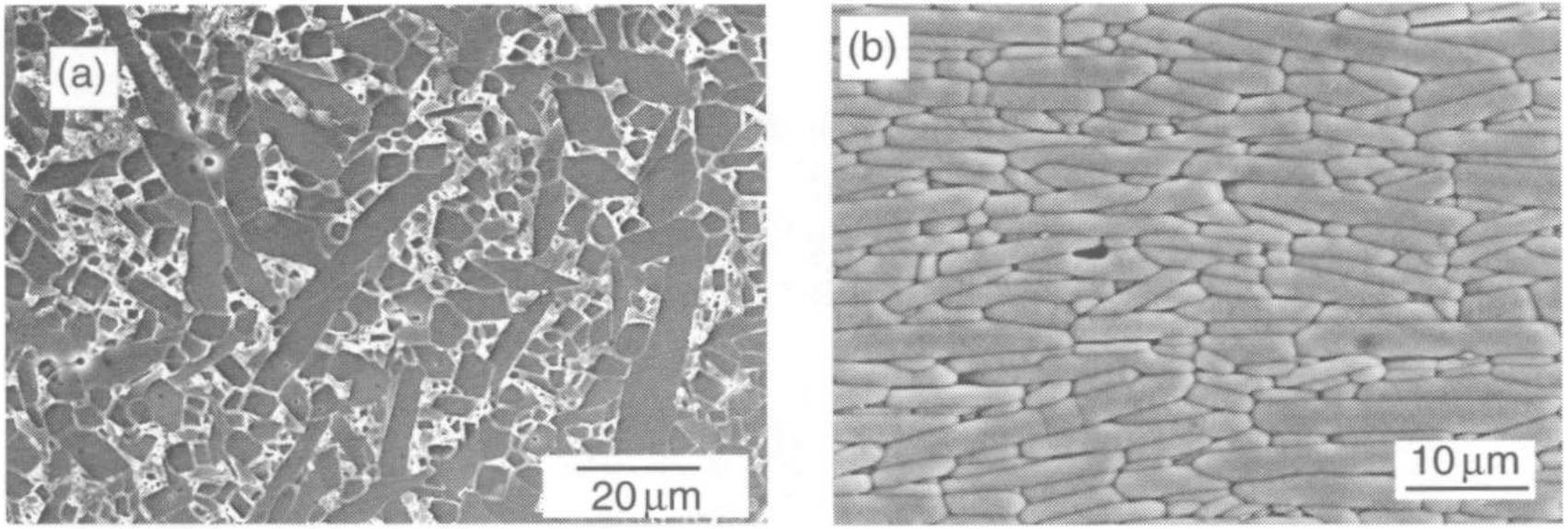

FIGURE 4.1.10 Exploitation of abnormal (anisotropic) grain growth for the production of (a) self-reinforced mullite with enhanced fracture toughness and (b) bismuth titanate ceramic with anisotropic dielectric properties.

Ostwald Ripening

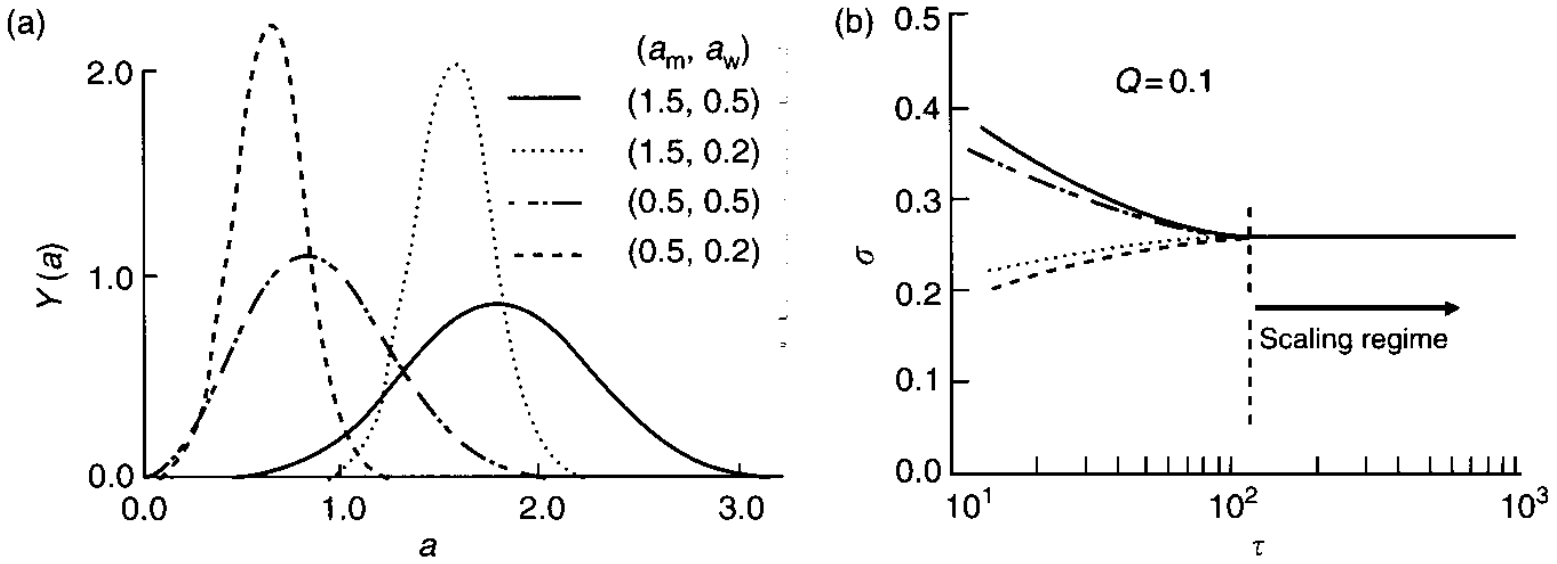

FIGURE 4.1.11 Effect of initial particle size distribution (a) on the time variation of the standard deviations of the distribution and the rate-coarsening rate (b) (after Ref. [84], with kind permission of Elsevier, Oxford).

In either case, the theory predicts that at some later time, a *self-similar* (steady-state) particle size distribution is approached asymptotically in which the growth of the critical radius, r^*, follows a simple law of the form given earlier by Eq. 15 for normal grain growth:

$$(r^*)^m = (r_0^*)^m + Kt$$

where K is a temperature-dependent rate constant, t is the time, and m is an exponent that depends on the rate-controlling mechanism: $m = 3$ for diffusion control and $m = 2$ for surface reaction control.

Control of Grain Growth

TABLE 4.1.2 Examples of Dopants Used for Grain Growth Control in Some Common Ceramics

Host	Dopant	Concentration (at %)	Reference
Al_2O_3	MgO	0.025	[63, 93]
$BaTiO_3$	Nb; Co	0.5–1.0	[94, 95]
ZnO	Al	0.02	[96]
CeO_2	Y; Nd; Ca	3–5	[91, 92]
Y_2O_3	Th	5–10	[97]
SiC	(B + C)	0.3B + 0.5C	[98]

Solute drag

In the solute drag theory put forward by Cahn [90], the boundary mobility of the doped material is given by

$$M'_b = \frac{D_b \Omega}{4kT\delta_{gb} Q C_0} \qquad (19)$$

where D_b is the diffusion coefficient for the solute atoms across the boundary of width δ_{gb}, Ω is the atomic volume of the host atoms, k is the Boltzmann constant, T is the absolute temperature, Q is a partition coefficient for the solute distribution between the boundary and the lattice, and C_0 is the concentration of the solute atoms in the lattice.

The Zener formula

According to Zener, the matrix reaches a limiting grain size given by

$$G_{max} = \frac{2\alpha r}{3f} \qquad (20)$$

where α is a geometrical constant that depends on the shape of the matrix grains, r is the radius of the precipitates (assumed to be spherical), and f is the volume fraction of the precipitates.

Grain Growth and Pore Evolution in Porous Compacts

Interaction between Pores and Grain Boundaries

For each of the mechanisms indicated in Figure 4.1.12, analysis of the atomic flux from the leading surface of the pore to the trailing surface yields a pore mobility, M_p, of the form [53]:

$$M_p = \frac{AD\Omega}{kTr^n} \tag{21}$$

where A is a constant, Ω is the atomic volume, k is the Boltzmann constant, T is the absolute temperature, r is the radius of the pore, D is the appropriate diffusion coefficient, and m is an exponent that depends on the mechanism: $D = D_s$ and $m = 4$ for surface diffusion; $D = D_l$ and $m = 3$ for lattice diffusion; $D = D_g$ and $m = 3$ for vapor transport.

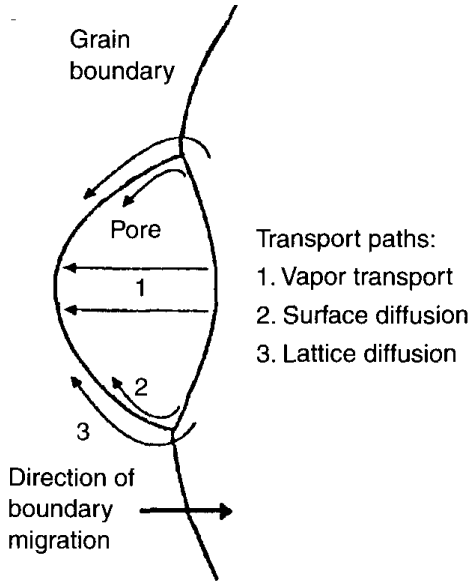

Possible transport paths for a pore moving with a grain boundary.

Microstructural Maps

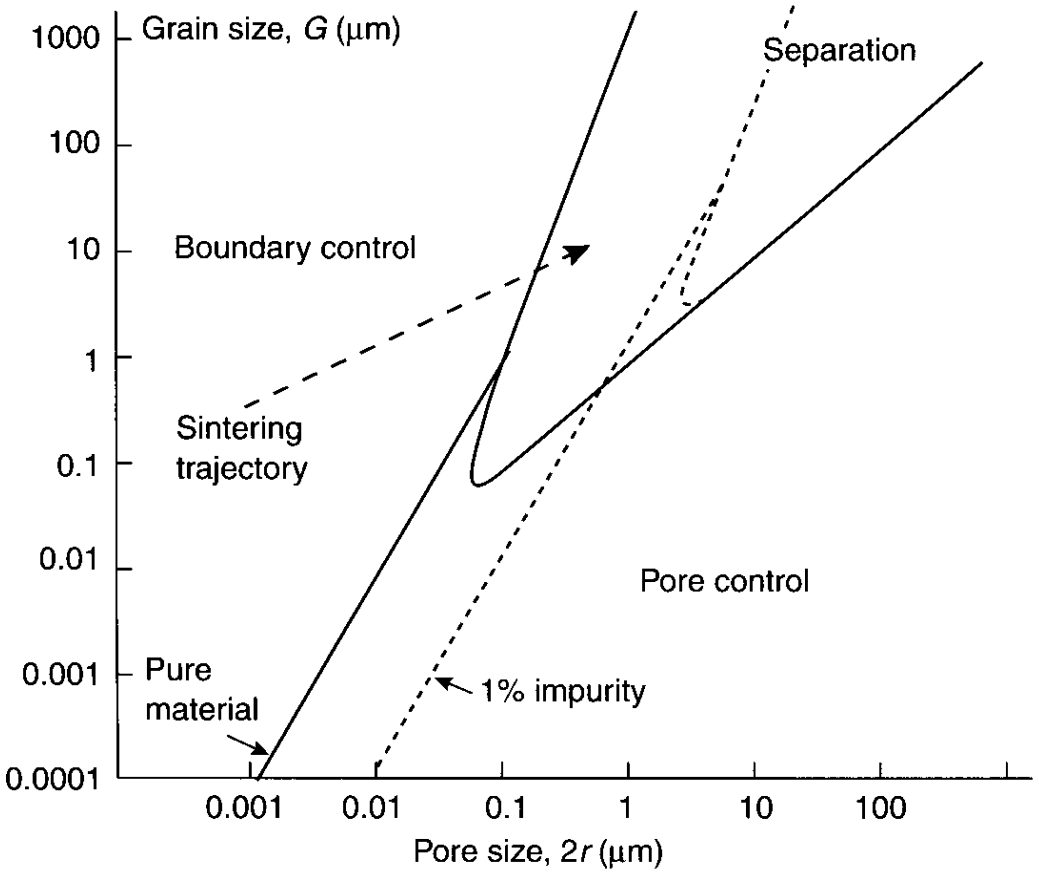

Grain size versus pore size map showing the conditions for pore attachment and pore separation. A trajectory for densification accompanied by coarsening of the microstructure is shown. If the separation region is not intersected, then the attainment of complete densification is possible (from Ref. [109], with kind permission of Elsevier, Oxford).

Microstructural Maps

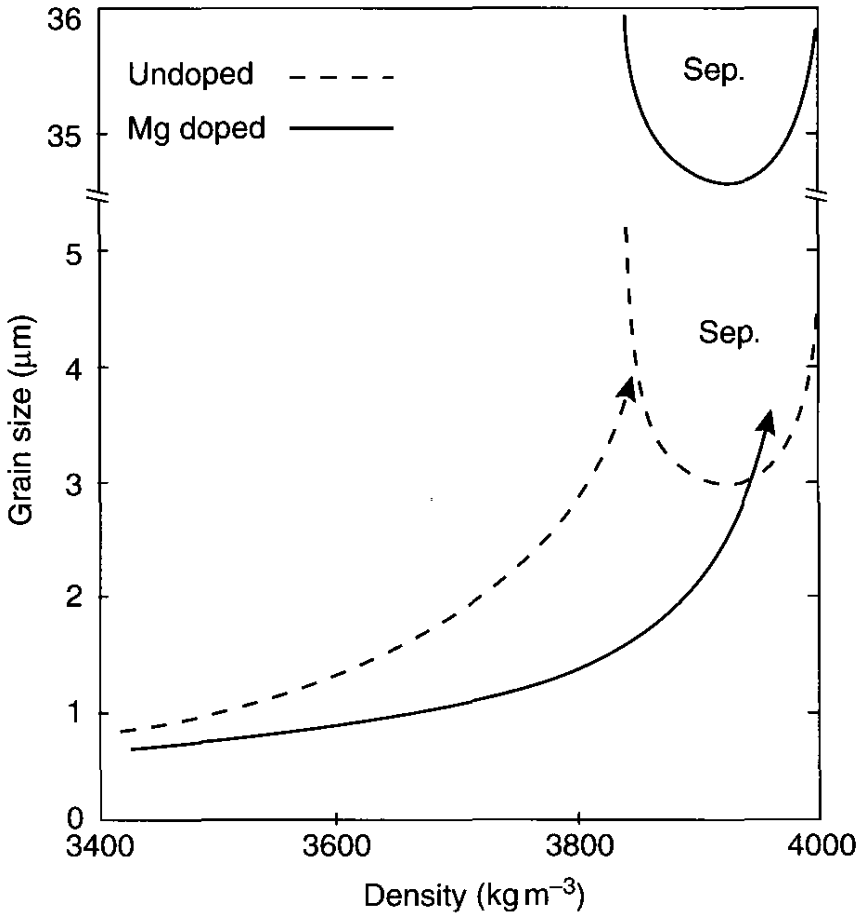

Grain size versus density map for undoped Al_2O_3 and for Al_2O_3 doped with 250 ppm MgO. The depicted trajectory for the doped Al_2O_3 is the result of raising the surface diffusivity by a factor of 4, reducing the lattice diffusion coefficient by a factor of 2, and reducing the grain boundary mobility by a factor of 34 (courtesy of M. P. Harmer).

LIQUID-PHASE SINTERING

Some Liquid-Phase Sintering Systems

System	Reference
Alumina + $Mg_3Si_4O_{10}(OH)_2$ (talc)	[113]
$ZnO + Bi_2O_3$	[114]
$SiC + Y_2O_3 + Al_2O_3$	[115]
Si_3N_4 + MgO, Sialons	[116, 117]
$BaTiO_3 + B_2O_3$	[118]

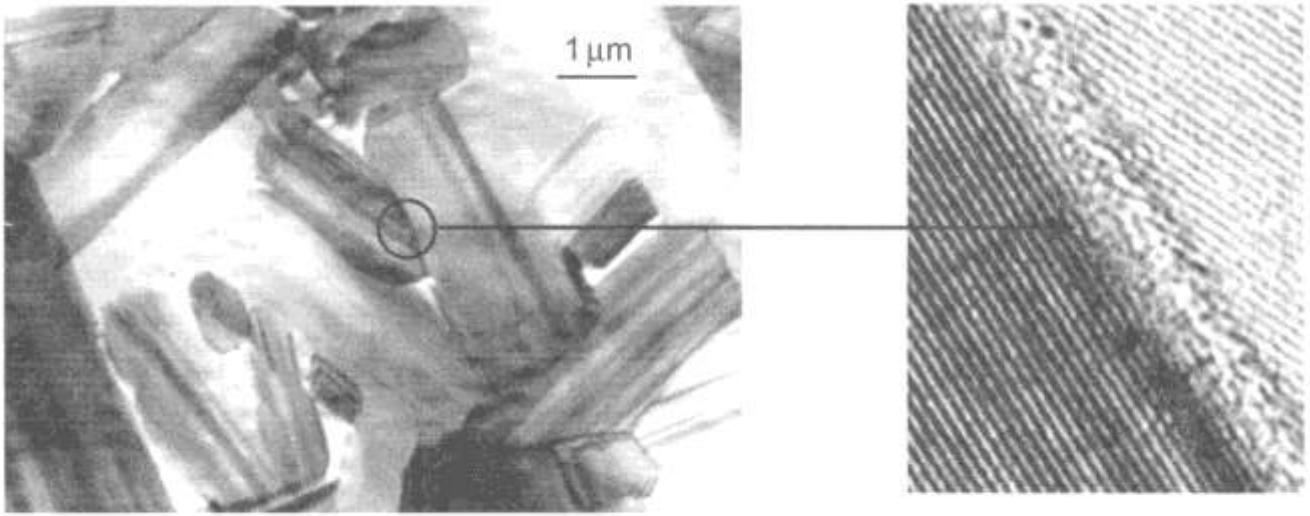

Persistent amorphous grain boundary phase, approximately 1-nm thick, in SiC containing Al, B and C as sintering additives (from Ref. [122]).

LIQUID-PHASE SINTERING

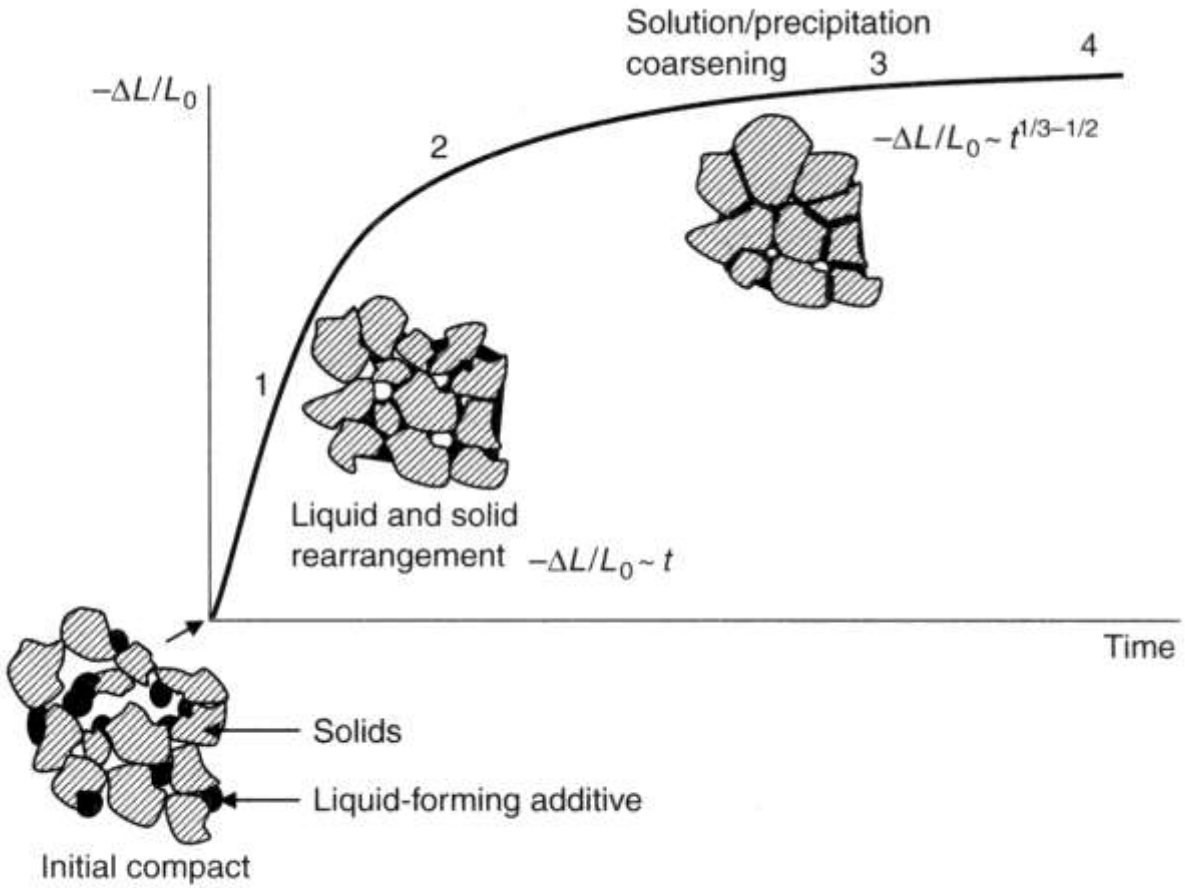

Tens.

Schematic evolution of powder compact during liquid-phase sintering. The various stages are overlapping significantly.

Redistribution of the liquid and rearrangement of the particulate solid under the influence of capillary stress gradients
Densification and grain growth by solution-precipitation
Final-stage sintering dominated by Ostwald ripening

Liquid-phase redistribution

The dihedral angle, ψ, is related to the solid/liquid interfacial energy, γ_{sl} and the grain boundary energy γ_{gb} by the vector force balance, similar to Eq. 5:

$$2\gamma_{sl}\cos(\psi/2) = \gamma_{gb}$$

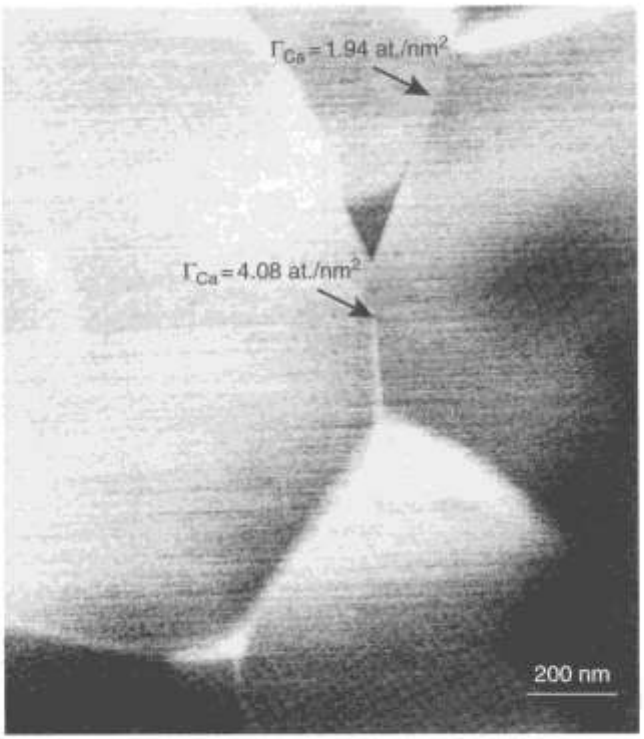

STEM image showing two neighboring grain boundary films with remarkably different calcium excess in calcia-doped silicon nitride (from Ref. [125]).

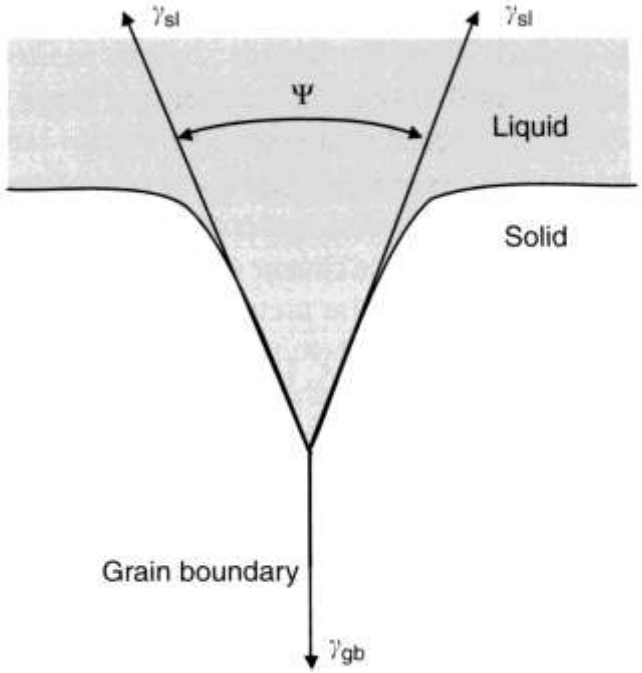

Dihedral angle for liquid at a grain boundary.

Morphology of liquid phase in the microstructure of polycrystals

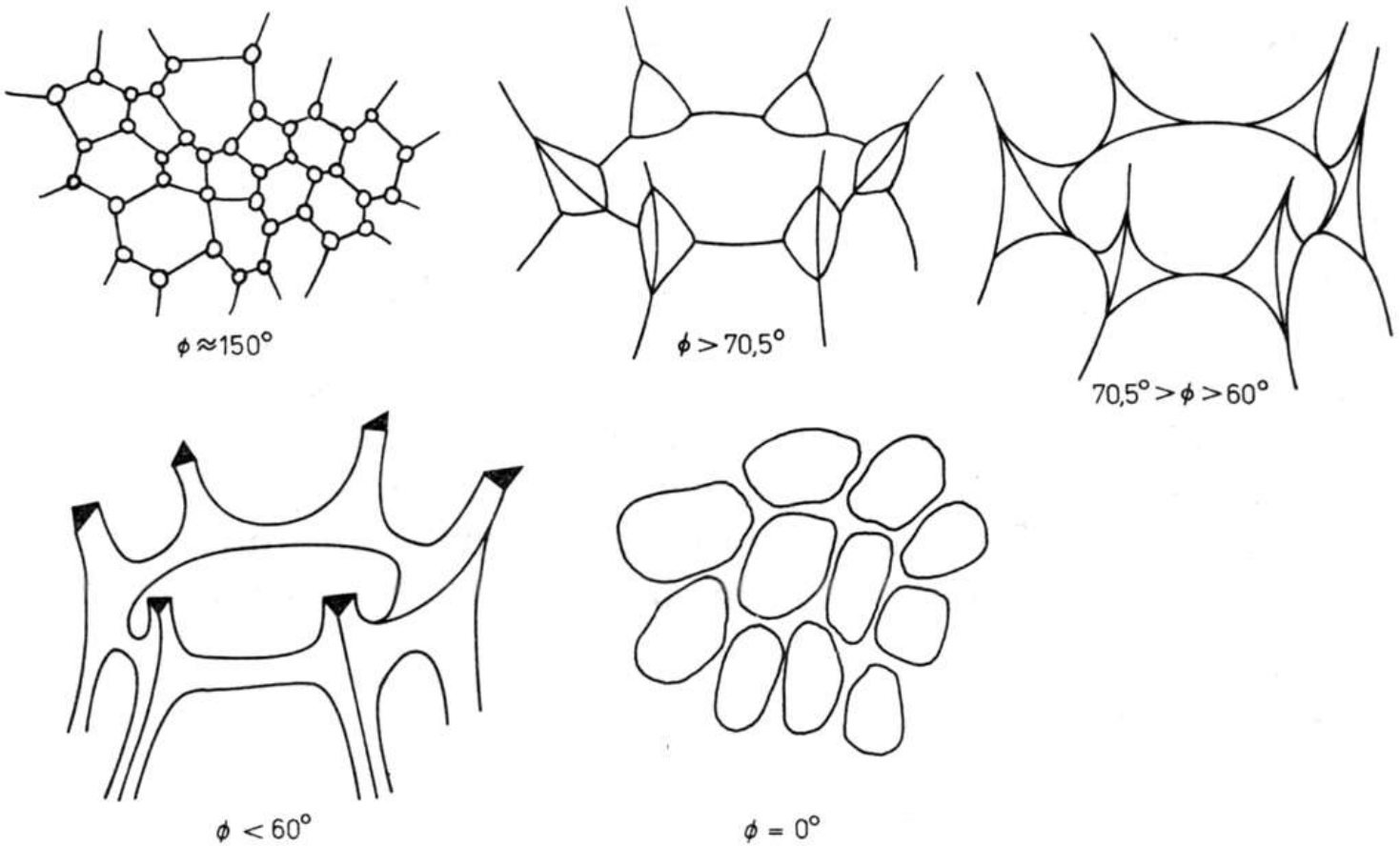

Dihedral angle dependence of liquid phase distribution

Effects of Gravity

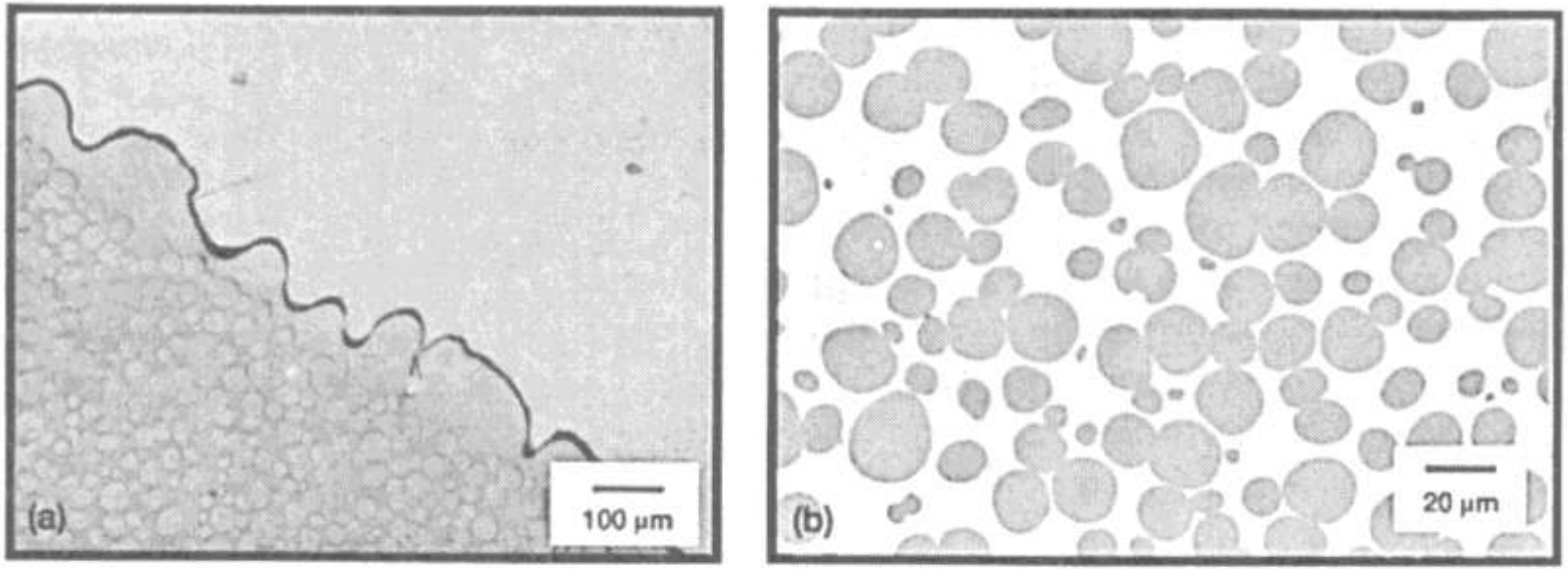

Micrographs of 78W–15.4Ni–6.6Fe after liquid-phase sintering for 1 min in microgravity at 1507°C: (a) low magnification view of sample edge and wavy solidified liquid; (b) high magnification view of sample interior showing solid grain agglomeration (courtesy R. M. German).

Grain Boundary Films

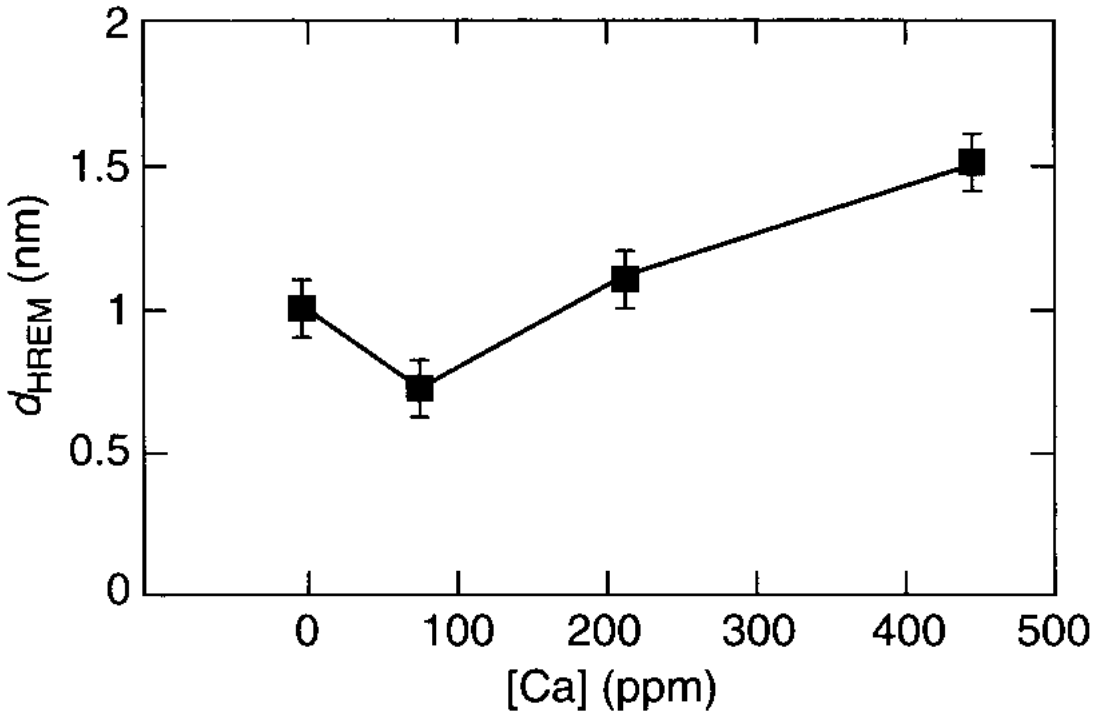

Equilibrium grain boundary thickness measured by HREM (d_{HREM}) plotted against bulk calcium doping level in silicon nitride (from Ref. [133]).

Effective Stress

Concepts that have been developed in soil mechanics [134, 135] can also be applied to liquid-phase sintering. Considering a cross-section that runs through the particle–particle contacts, the particle network, or skeleton, will carry an effective stress given by

$$\sigma_y^{\text{eff}} = \left(\sum F_{iy}\right)/a$$

where F_{iy} is the component of the force in the y direction at the ith particle–particle contact, and a is the external cross-section of the sample. In the absence of any externally applied stress and pressure gradients, the effective stress is then

$$\sigma_y^{\text{eff}} = p(1 - a)$$

where p is the capillary pressure in the liquid phase.

Role of the Wetting Angle

The wetting angle, θ, for the liquid/solid/vapor system depends on the various interfacial energies, and is usually referred to a droplet of liquid on a flat solid surface. While this does not represent the full equilibrium, it is often cited as such, and is given by

$$\cos\theta = (\gamma_{sv} - \gamma_{sl})/\gamma_{lv}$$

where γ_{sv}, γ_{sl}, and γ_{lv} are the specific energies of the solid/vapor, solid/liquid, and liquid/vapor interfaces, respectively.

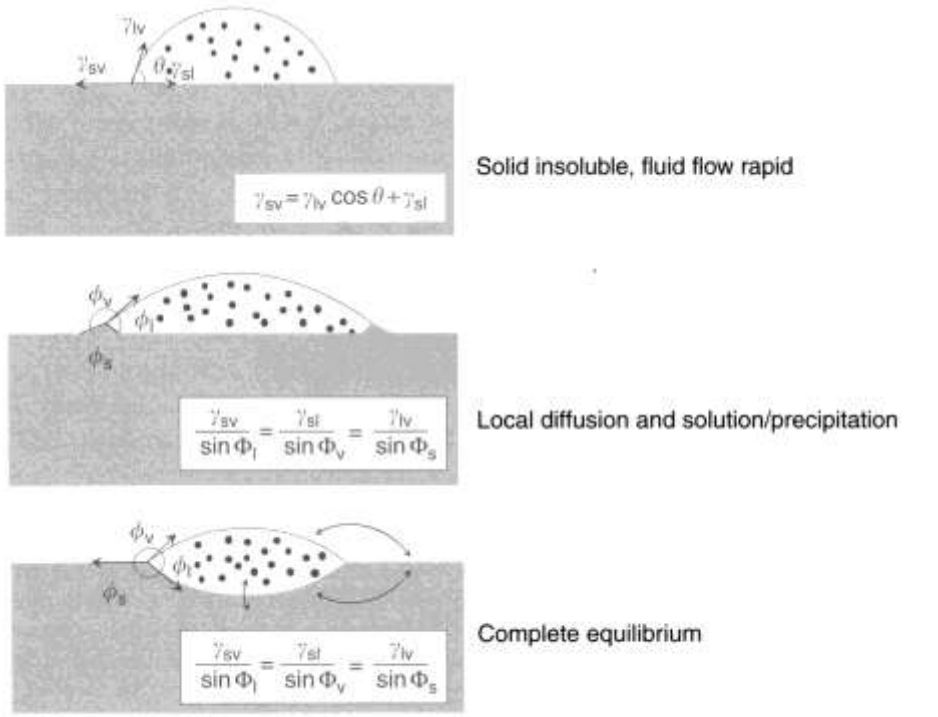

Shape changes associated with partial solubility of the solid in the liquid [140] (courtesy R. M. Cannon).

Relative Amount of Liquid Phase

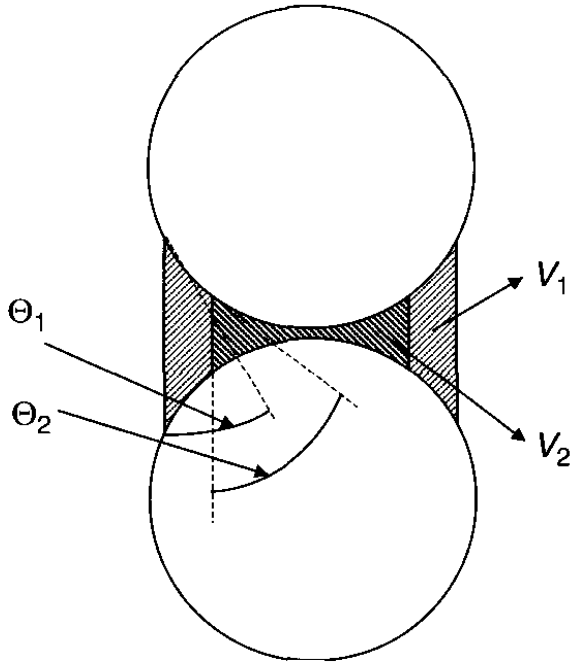

Two-dimensional illustration of the dependence of the neutral volume of liquid phase for a two-particle geometry. At fixed particle separation the neutral conditions will depend on the equilibrium contact angles Θ_i, and the corresponding liquid volumes V_i. With decreasing contact angle, the neutral liquid volume increases. The exact neutral condition in three dimensions still involves some liquid surface curvature when viewed in a two-dimensional section. A liquid volume in excess of the neutral volume produces a repulsive condition between the particles.

Reaction Sintering

Some Reaction Sintering Systems

Reactant powders	Resulting ceramic	Reference
$3Al_2O_3 + 2ZrSiO_4$	$3Al_2O_3 + ZrO_2$	[147]
$Si_3N_4 + AlN + Al_2O_3$	Sialon	[148]
$SiO_2 + Al_2O_3$	Mullite	[149]
$ZnO + Al_2O_3$	$ZnAl_2O_4$	[150]

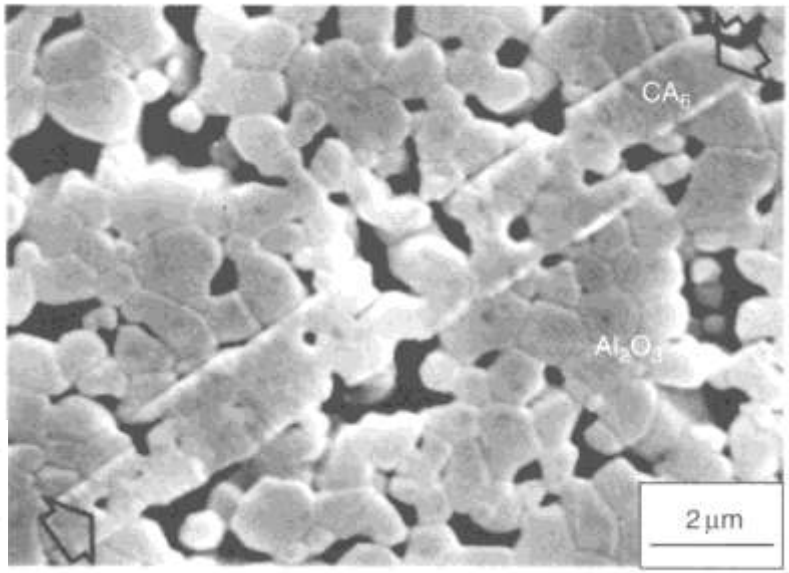

Scanning electron micrograph of calcium hexa-aluminate (CA_6 arrowed) formed during the densification of alumina powder mixed with 5 wt% particulate CaO, after 20 h at 1330°C. The plate-shaped CA_6 phase replicates the porous alumina matrix during solid-state reaction/grain growth (from Ref. [120]).

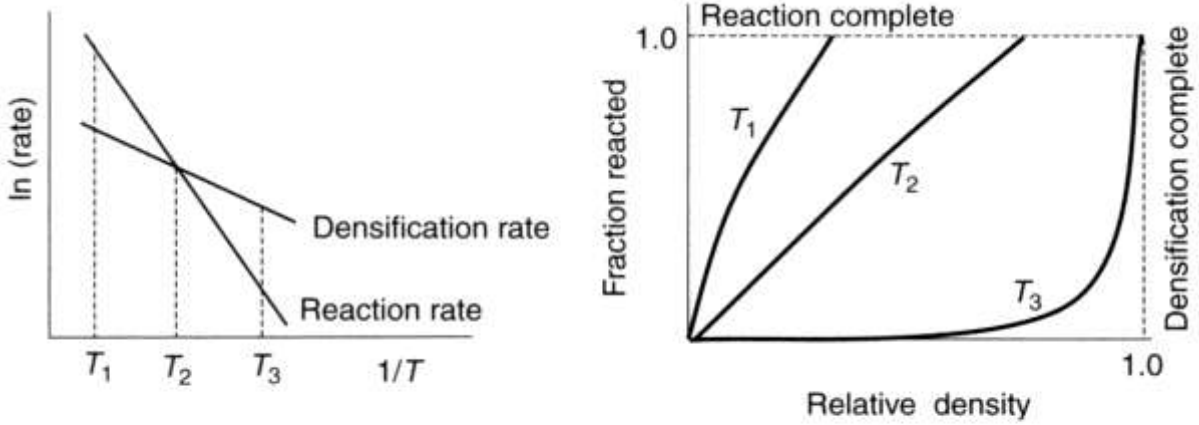

Schematic relationship between densification rate and reaction rate as a function of temperature T, and the resulting process trajectory. If the reaction rate is fast compared to densification, complete reaction can occur with limited densification (after Ref. [147]).

Influence of Processing Parameters

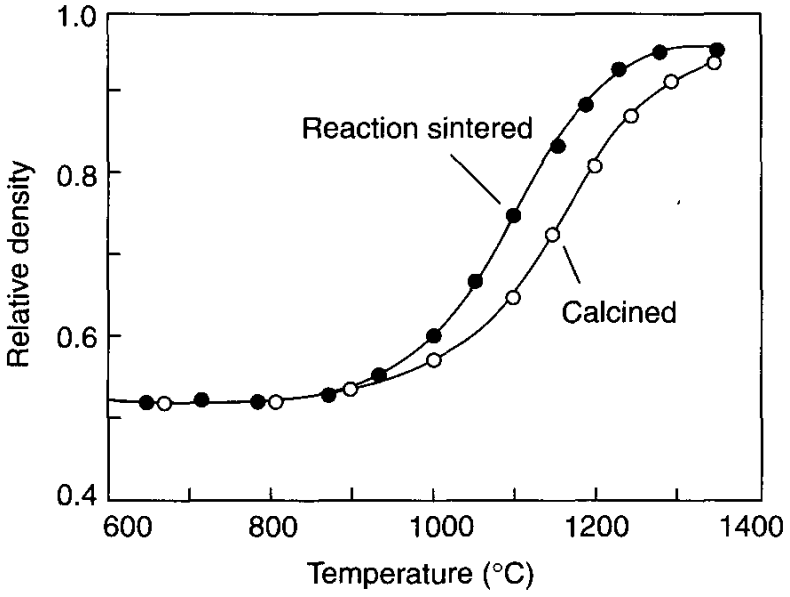

Relative density versus temperature for sintering of $ZnO–Fe_2O_3$ powder mixtures and for pre-calcined powders of $ZnFe_2O_4$ (from Ref. [155]).

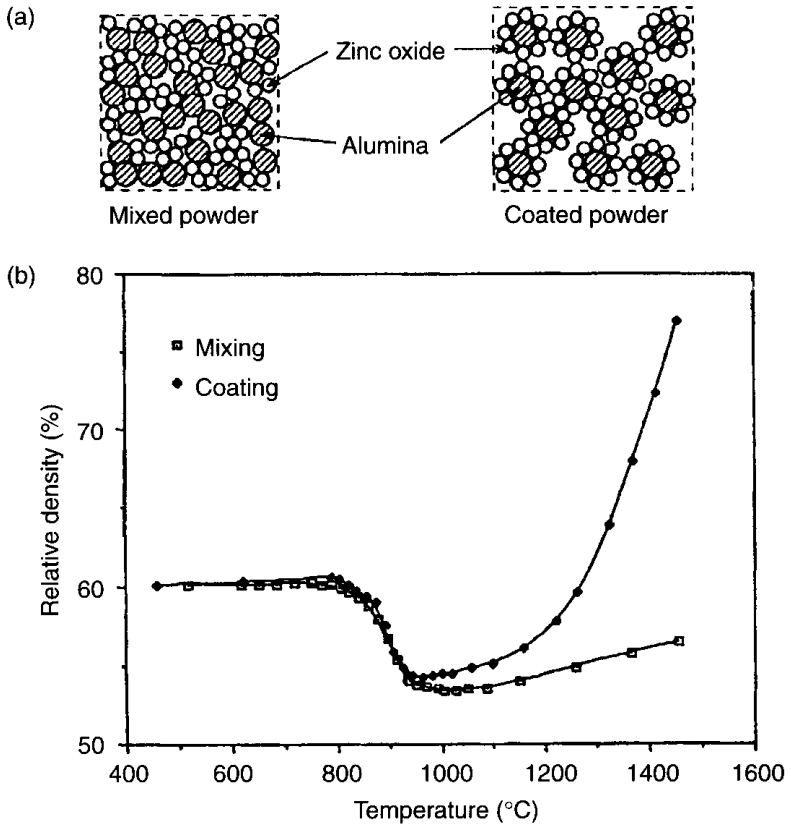

Effect of reactant powder distribution on densification for reaction sintering of $ZnO–Al_2O_3$. Considerably more densification results for coated powders (from Ref. [156]).

Sintering with etching o polycrystalline particles

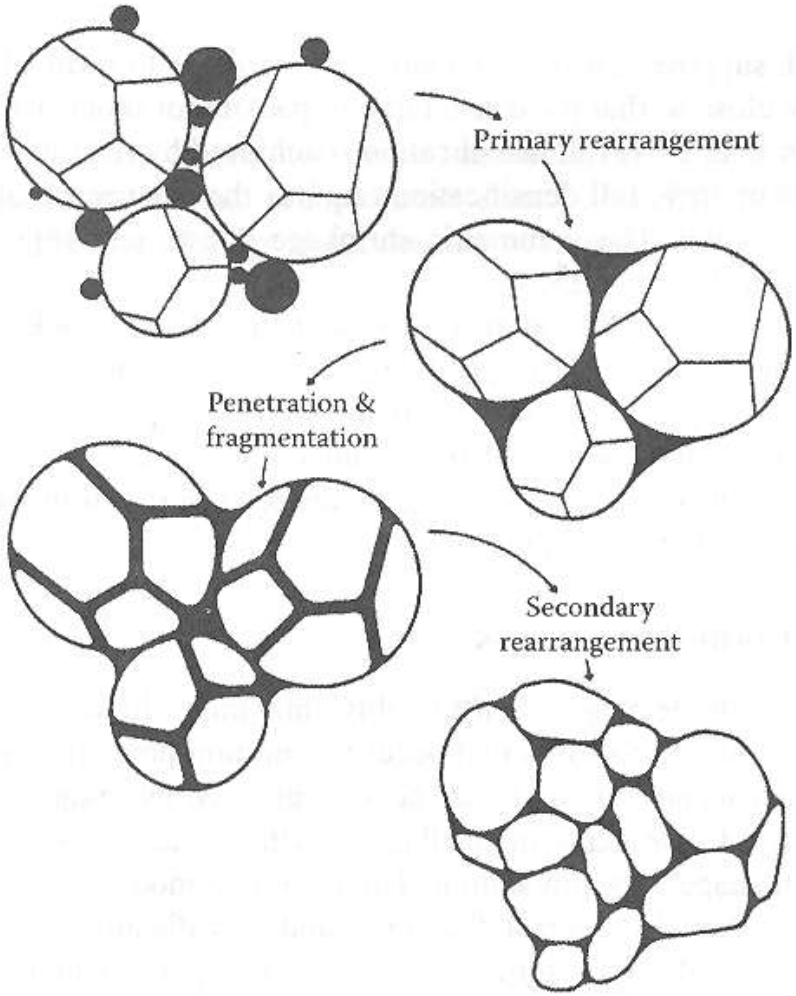

Schematic diagram illustrating fragmentation and rearrangement of polycrystalline particles.

CONSTRAINED SINTERING

Disperced Inert Phases

However, the system is basically near the viscous limit, predicting relatively small back stresses. Scherer's analysis [158] leads to a linear densification rate of the composite, $\dot{\varepsilon}_c$, that follows from the free (i.e. unconstrained) densification rate of an identical matrix, $\dot{\varepsilon}_{fm}$, predicted by

$$\dot{\varepsilon}_c = [(1-f)K_{cs}/4G_m]\dot{\varepsilon}_{fm}$$

where f is the volume fraction of the inert inclusions, and K_{cs} is related to the shear viscosity, G_m, and the bulk viscosity, K_m, of the matrix is given by $K_{cs} = 1/(1/4G_m + f/3K_m)$.

Another way of expressing the results is to invoke the densification rate of the composite as predicted by a simple, linear rule of mixture, which for an inert and uniformly dispersed inclusion phase would be

$$\dot{\varepsilon}_c^{rm} = (1-f)\dot{\varepsilon}_{fm}$$

Combining Eqs 26 and 27 leads to

$$\dot{\varepsilon}_c/\dot{\varepsilon}_c^{rm} = 1/[1 + f(4G_m/3K_m)]$$

Supported Films

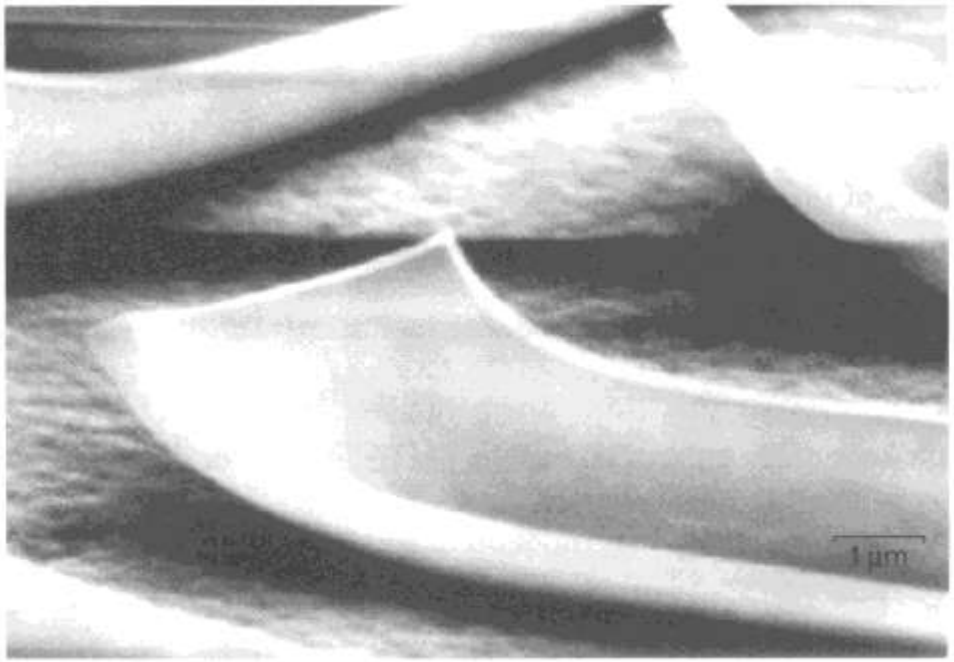

Delamination of a sintered zirconia thin film produced by sol–gel methods on a nanoporous (0.02 µm) alumina substrate (from Ref. [166]).

Sintering Practice

Heating Schedules

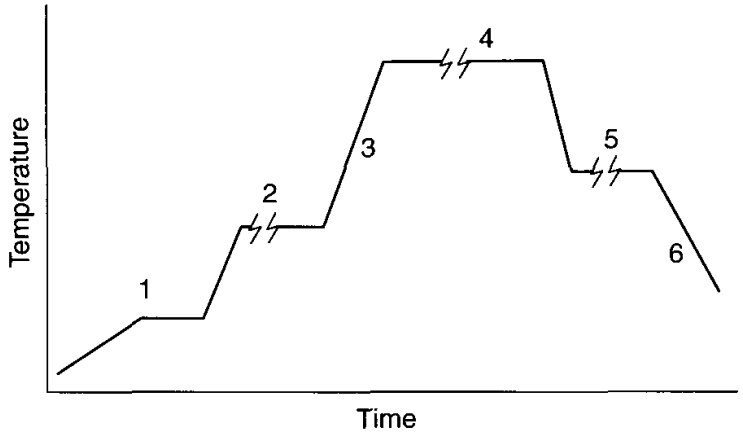

Generalized heating schedule.

Isothermal Sintering

Constant Heating Rate Sintering

Sintering Practice

Multi-stage Sintering

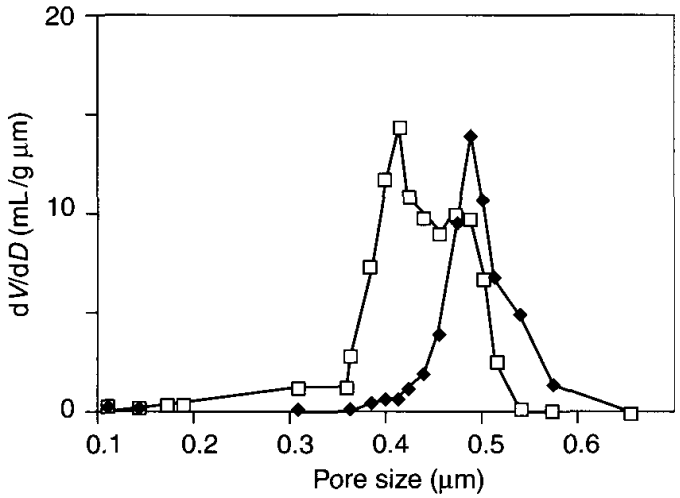

Pore size distribution narrowing after 50 h at 800°C for an alumina powder compact, determined by mercury porosimetry (from Ref. [177]).

Rate-Controlled Sintering

Fast-Firing

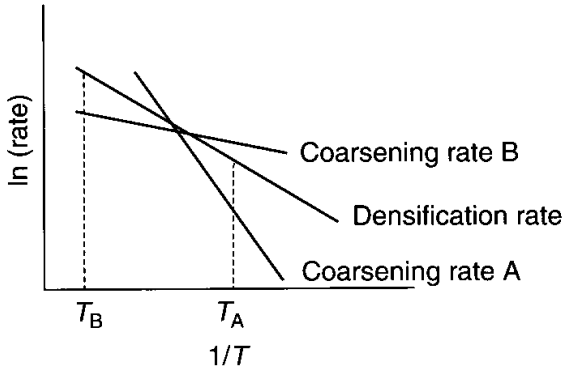

Possible relation of coarsening rates to densification rate. The preferred sintering temperatures T_A or T_B correspond to the coarsening rates A or B.

Sintering Practice

Microwave Sintering

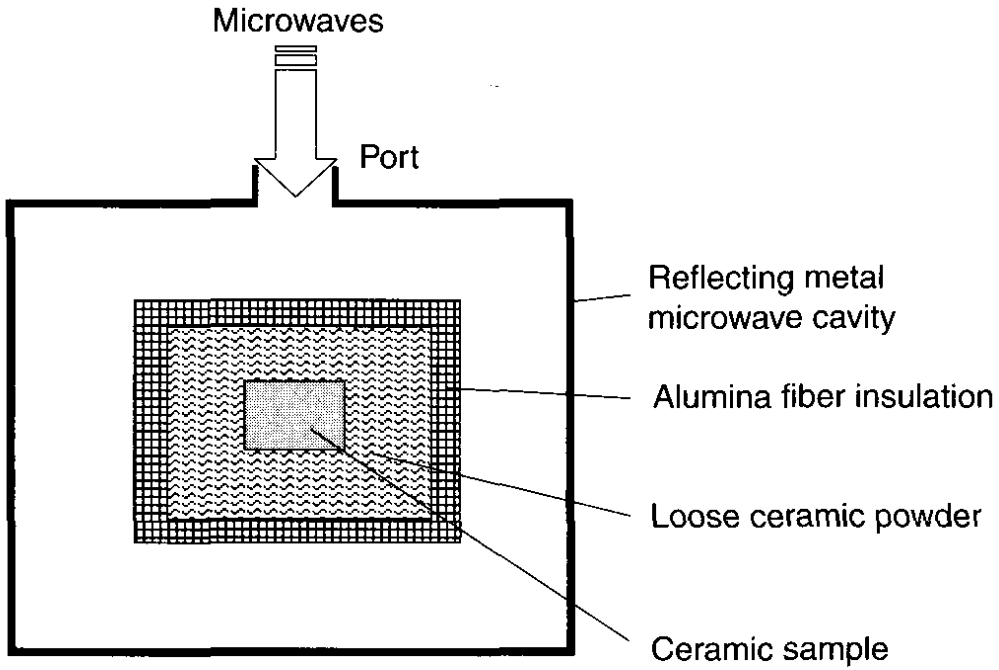

Schematic microwave sintering setup.

Sintering Practice

Plasma-Assisted Sintering

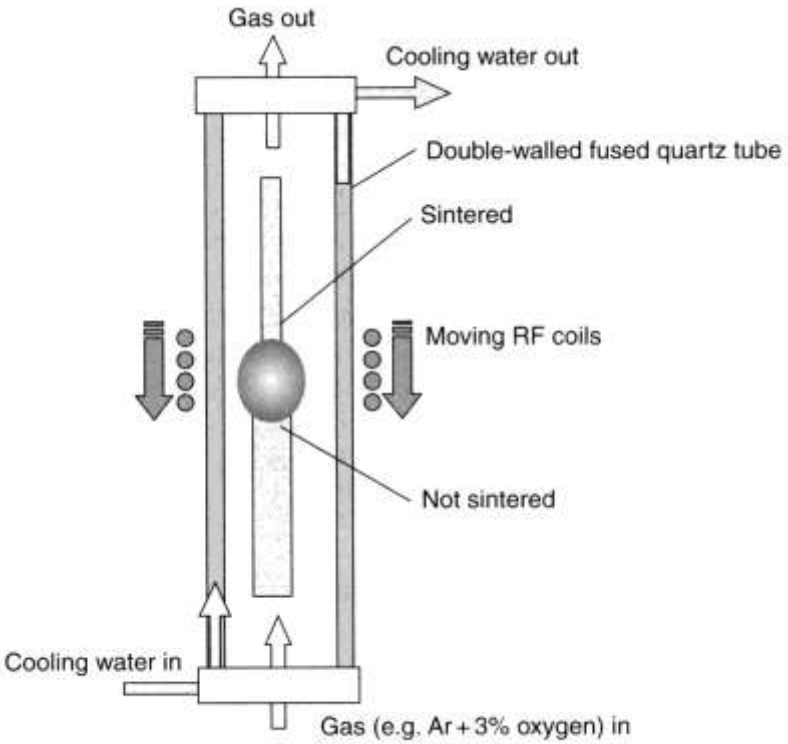

Schematic of plasma sintering setup.

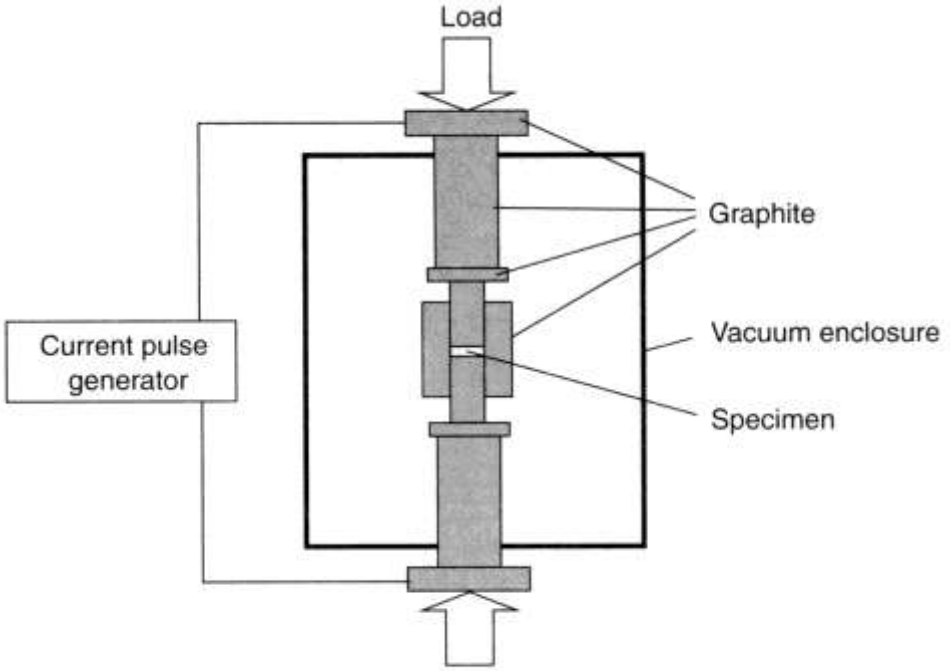

Schematic of a spark plasma sintering apparatus.

Pressure-Assisted Sintering

Hot pressing

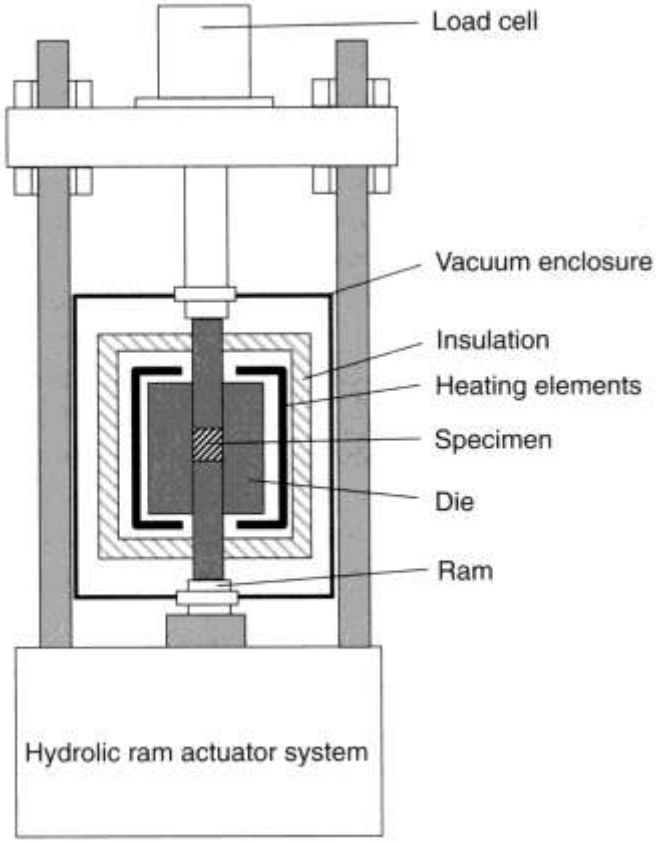

Schematic of the hot pressing process.

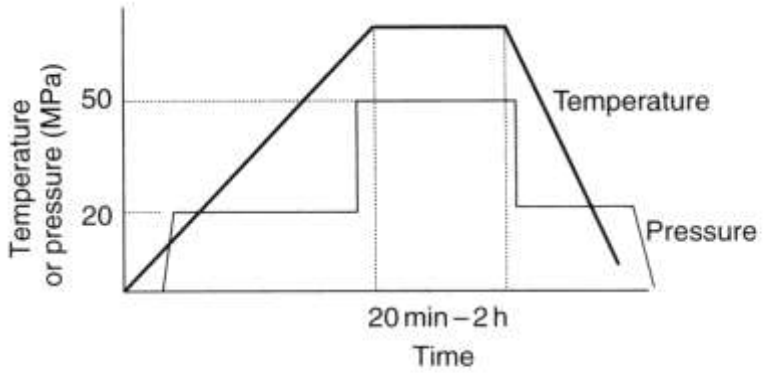

Schematic temperature/pressure schedule for hot pressing with a high-strength graphite die.

Pressure-Assisted Sintering

Sinter Forging

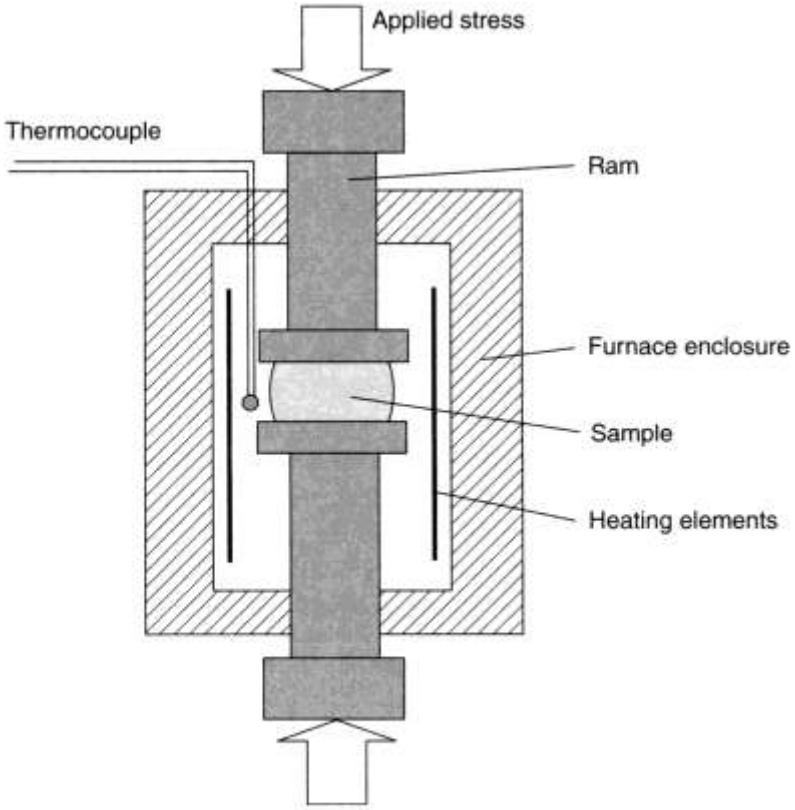

Schematic setup for sinter forging.

Pressure-Assisted Sintering

Hot Isostatic Pressing (HIPing)

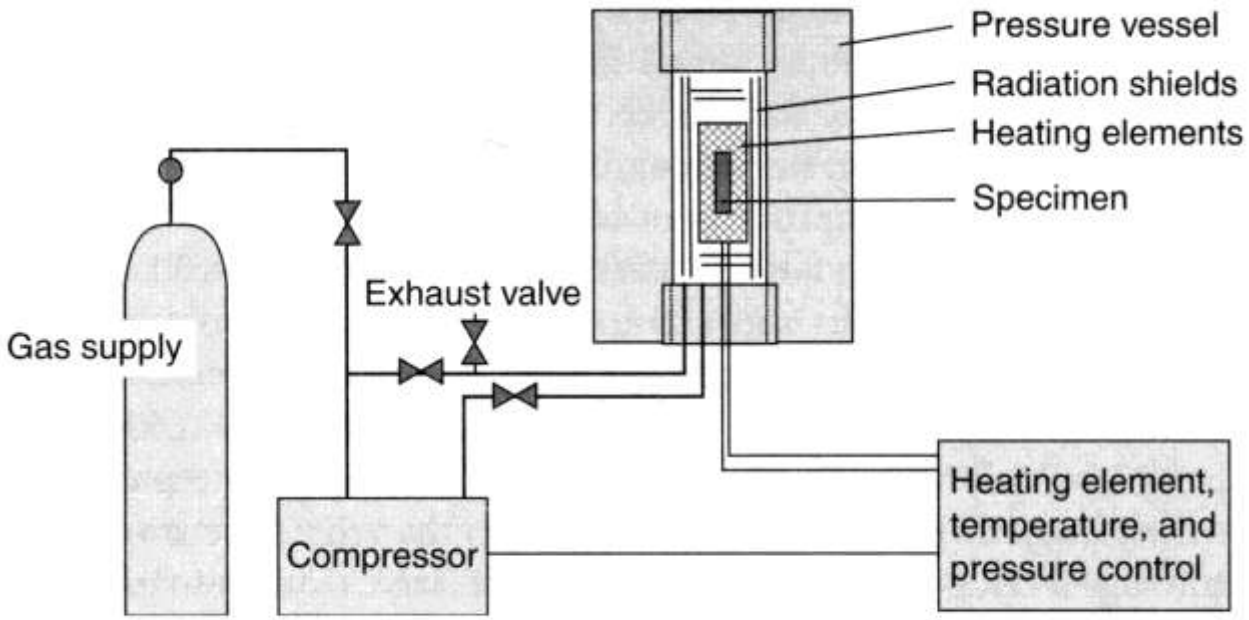

Schematic of hot isostatic pressing equipment.

Particle and Green Compact Characteristics

Particle size

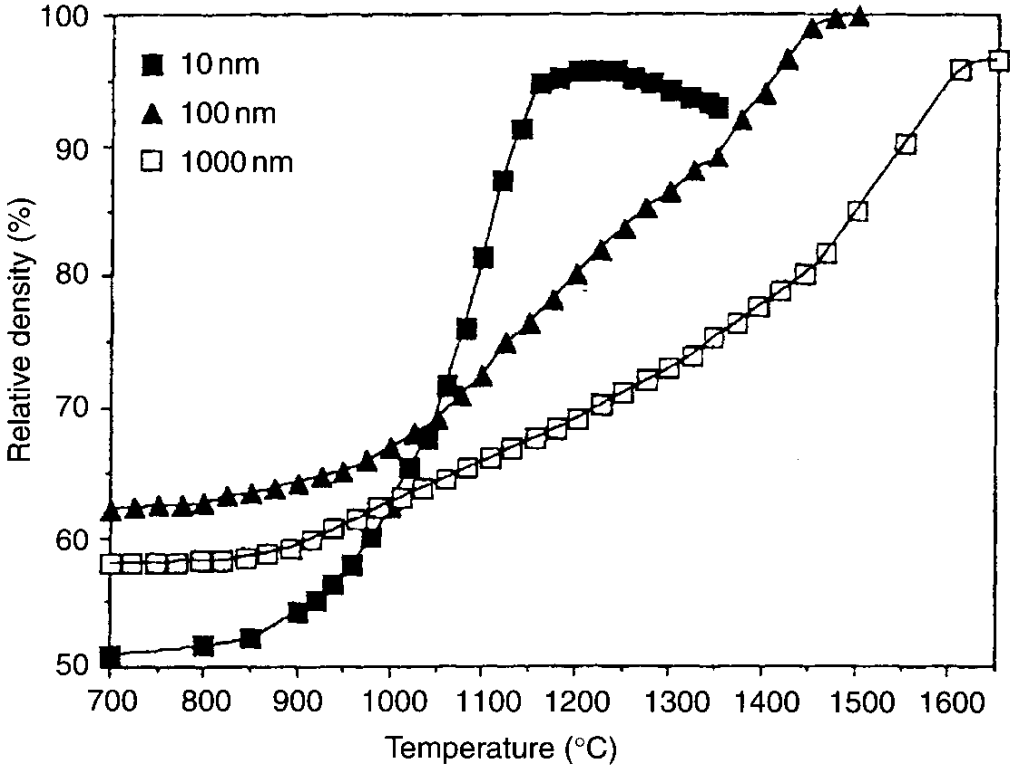

Effect of particle size on the sintering of CeO_2 powder compacts during constant heating rate sintering (10°C/min) in an oxygen atmosphere (from Ref. [207]).

Particle and Green Compact Characteristics

Particle Size Distribution

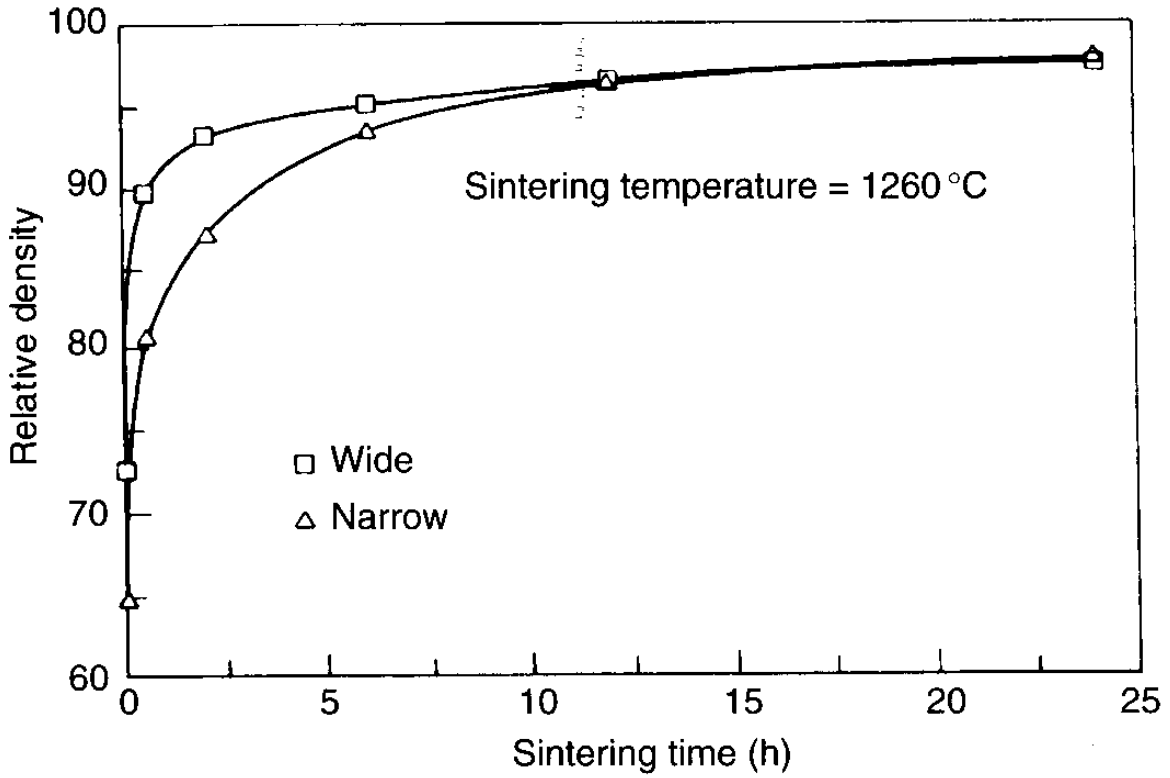

Effect of particle size distribution on the sintering of slip cast Al_2O_3 powder compacts prepared from wide and narrow size distribution powders having the same median particle size (from Ref. [228], with kind permission of American Ceramic Society).

Particle and Green Compact Characteristics

Particle Shape and Particle Structure

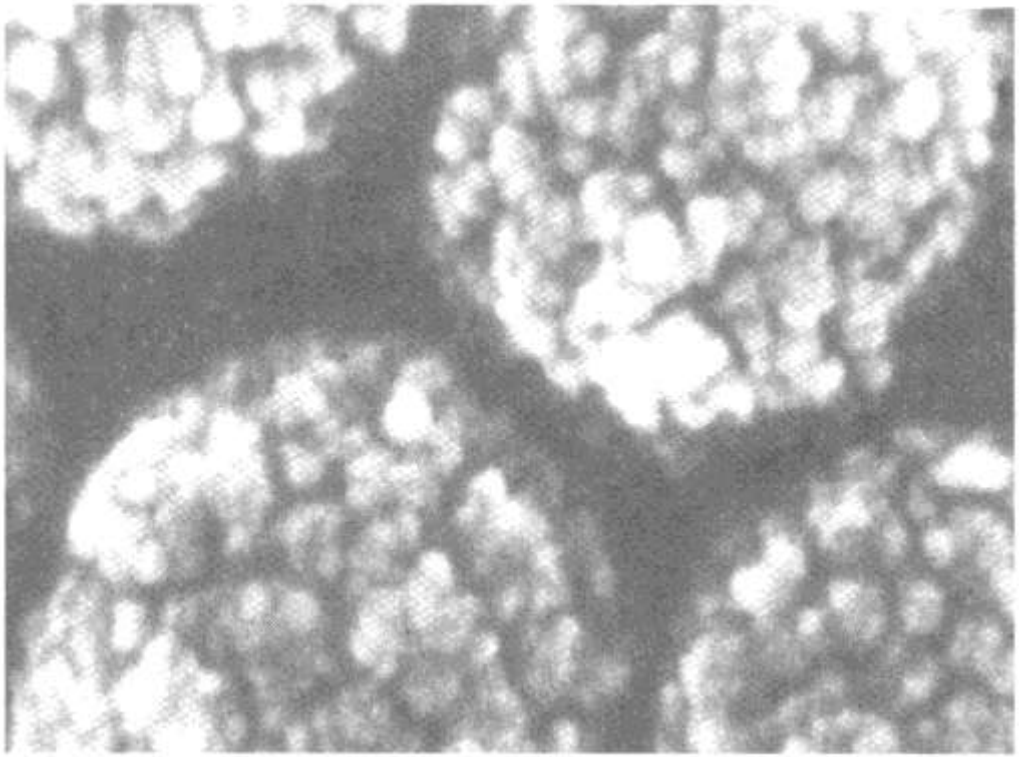

High-resolution SEM micrographs showing the substructure of monodisperse TiO_2 particles prepared by the Stober process. The spherical particles (~0.35 μm) consist of an aggregate of much finer particles (~10 nm) (courtesy of A. M. Glaeser).

Particle and Green Compact Characteristics

Particle Packing

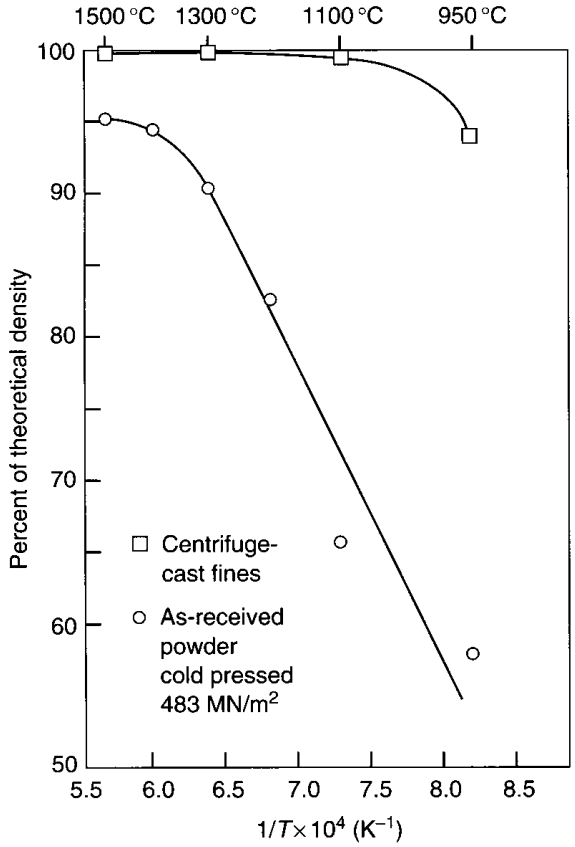

Effect of particle packing on the sintering of Y_2O_3-stabilized powder compacts after 1 h at various temperatures. The compact with the more homogeneous microstructure (formed by centrifugal casting of fine, agglomerate-free particles) reaches a significantly higher density than a compact formed by die-pressing the agglomerated, as-received powder (from Ref. [223], with kind permission of American Ceramic Society).

Differential densification

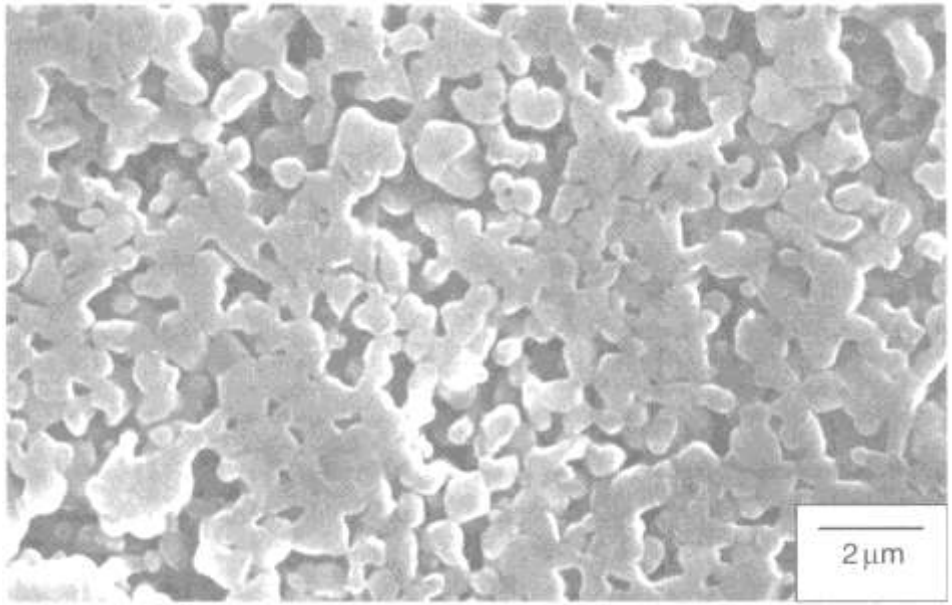

Differential densification during the sintering of an Al_2O_3 powder compact formed by die-pressing, leading to the development of denser and less dense regions.

Particle and Green Compact Characteristics

Effect of Green Density on Sintering

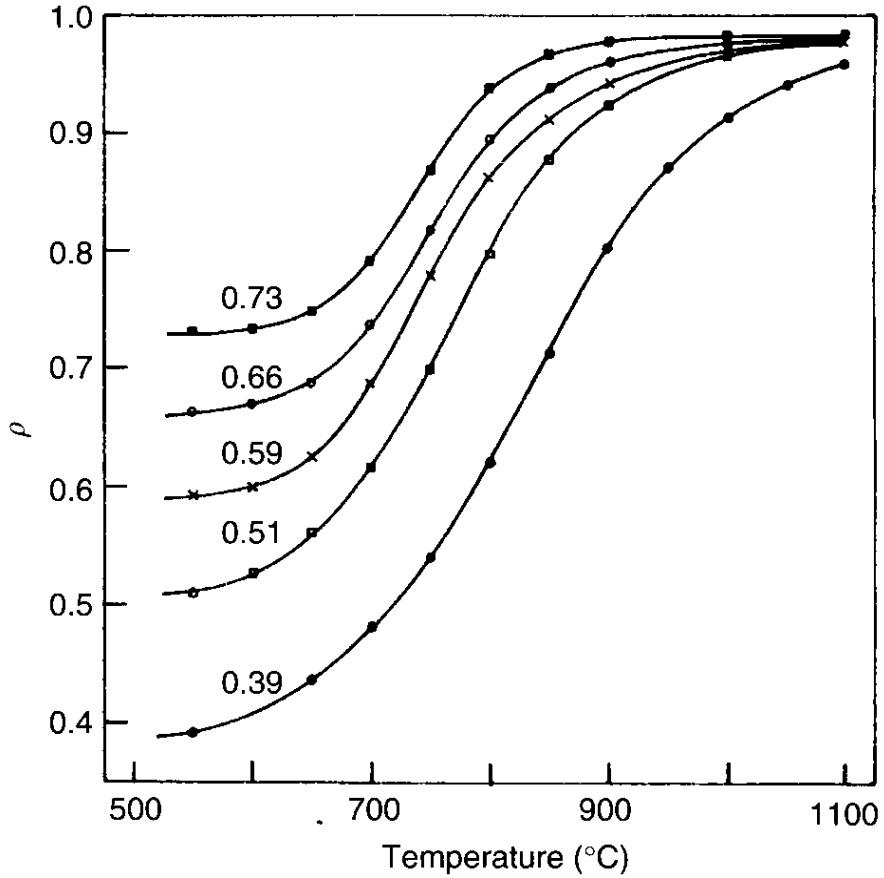

Effect of green density on the sintering of ZnO powder compacts during constant heating rate sintering (5°C/min) to 1100°C showing that for this powder, the final density is almost independent of the green density for a wide range of green density values (0.39–0.73) (from Ref. [37]).

CHEMISTRY CONSIDERATIONS

Gases in Pores

If it has a high solubility in the solid, the gas does not have a significant influence on sintering. For an insoluble gas, application of the gas laws shows that sintering stops when a limiting porosity, P_L, is reached, as given by

$$P_L = P_0 \left(\frac{p_0 r_0}{2\gamma_{sv}} \right)^{2/3}$$

where p_0 is the pressure of the sintering atmosphere, P_0 and r_0 are the porosity and radius, respectively, of the pores (assumed spherical in shape) when they become isolated, and γ_{sv} is the specific energy of the solid/vapor interface.

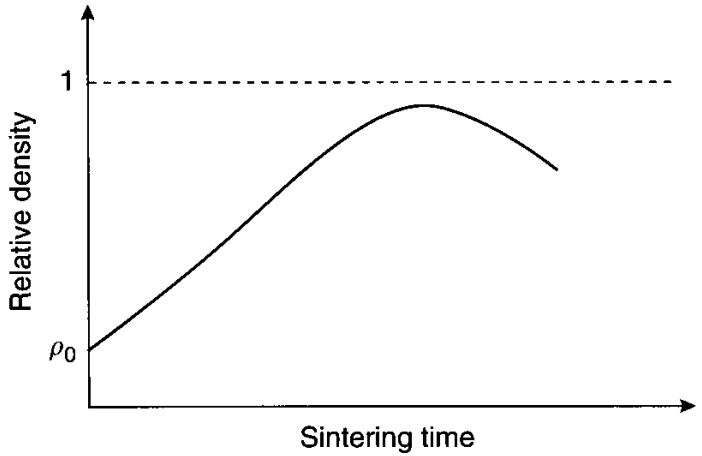

Schematic diagram illustrating the phenomenon of bloating produced by coarsening with gas-filled pores. The density decreases with time after reaching a maximum value.

CHEMISTRY CONSIDERATIONS

Vapor transport

$$Fe_2O_3\ (s) + 6HCl\ (g) \rightarrow Fe_2\ Cl_6\ (g) + 3H_2O\ (g)$$

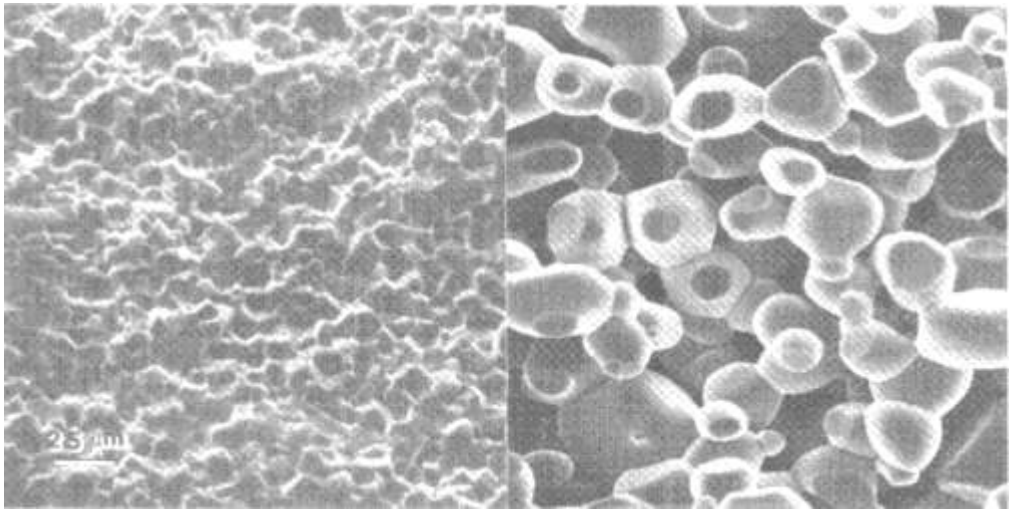

Scanning electron micrographs of fractured surfaces of Fe_2O_3 powder compacts sintered for 5 h in air (left) and in 10% HCl (right) (courtesy D. W. Readey).

Volatilization and Decomposition

$$PbO\ (s) \rightleftarrows PbO\ (g) \rightleftarrows Pb\ (g) + \tfrac{1}{2}O_2$$

$$Si_3N_4 \rightleftarrows 3Si\ (g) + 2N_2\ (g)$$

CHEMISTRY CONSIDERATIONS

Oxidation State

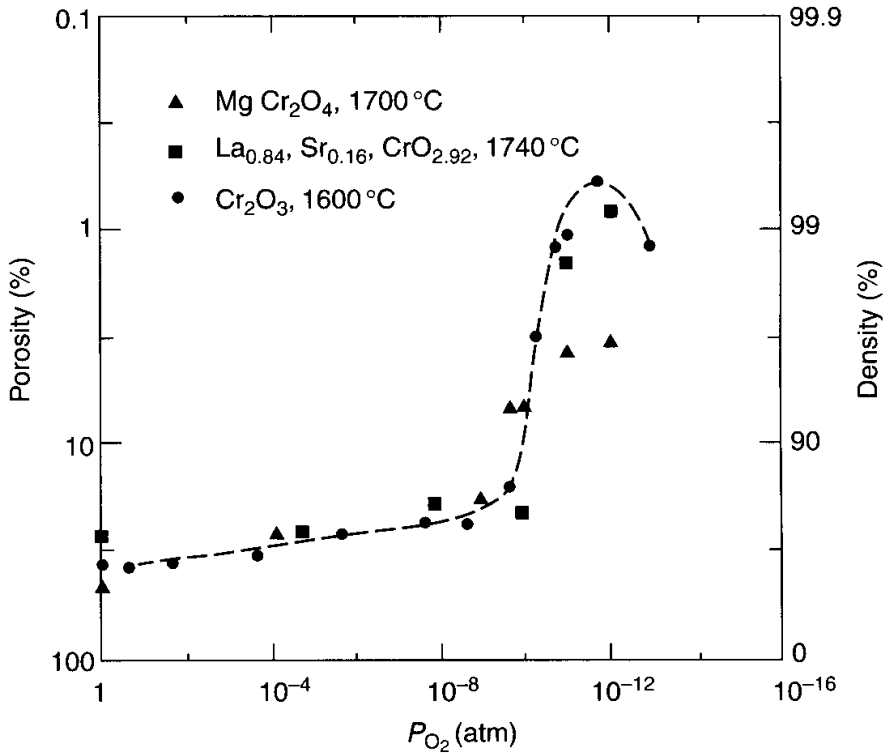

Dependence of porosity (or density) of sintered chromites on oxygen partial pressure in the sintering atmosphere (courtesy of H. U. Anderson).

CHEMISTRY CONSIDERATIONS

Defect chemistry and Stoichiometry

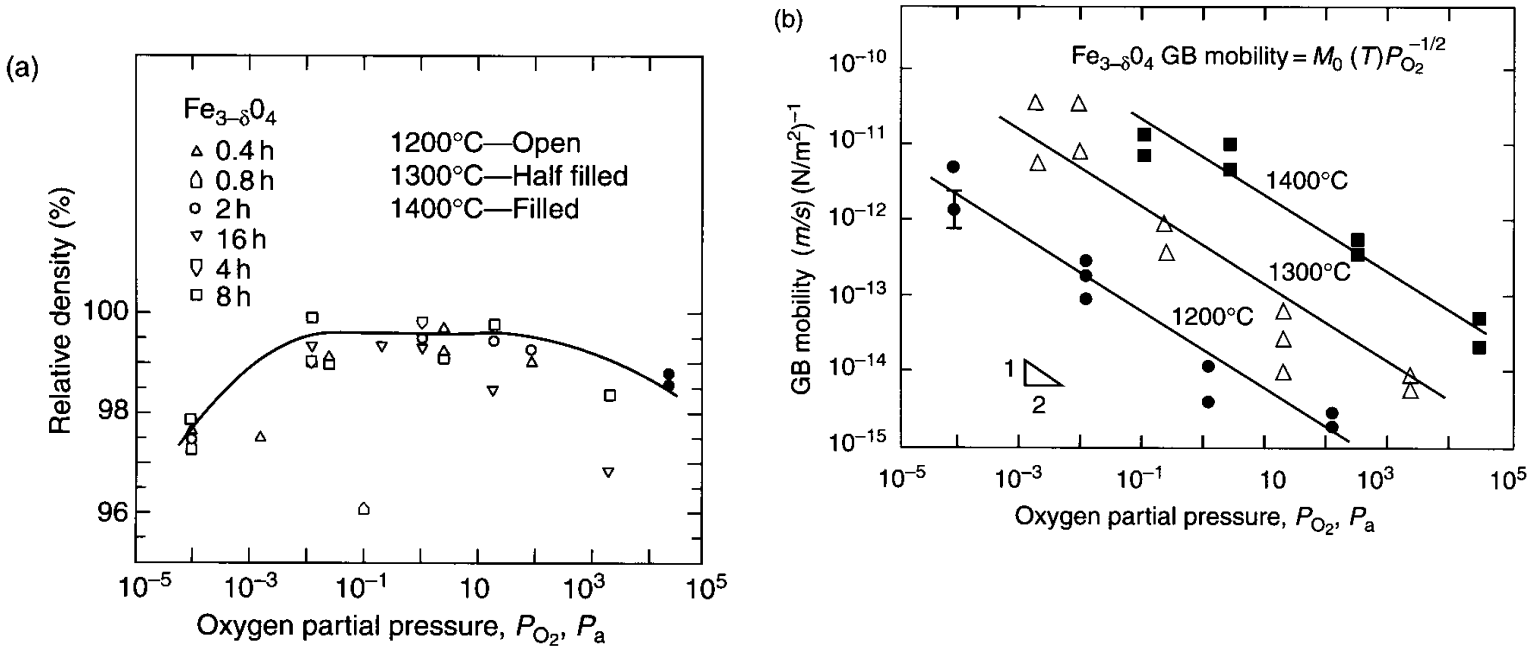

Data for (a) the relative density and (b) the boundary mobility as a function of the oxygen partial pressure in the atmosphere during the sintering of Fe_3O_4 powder compacts under the conditions of time and temperature indicated (from Ref. [257], with kind permission of American Ceramic Society).

Thank you for attention